$NdPO_4$ solubility and aqueous Neodymium speciation in supercritical fluids: An experimental study at 500-700 °C and 1.7 kbar

Debarati Banerjee[1*], Laura E. Waters[1], Nicole C. Hurtig[1], Alexander P. Gysi[1,2], Daniel Harlov[3,4,5], Chen Zhu[6], Artaches Migdisov[7]

[1] Dept. of Earth and Environment Science, New Mexico Institute of Mining and Technology, Socorro, NM 87801, USA

[2] New Mexico Bureau of Geology & Mineral Resources, New Mexico Institute of Mining and Technology, Socorro, NM 87801, USA

[3] Deutsches GeoForschungsZentrum GFZ Telegrafenberg, 14473 Potsdam, Germany

[4]Faculty of Earth Resources, China University of Geosciences, Wuhan 430074, China

[5]Department of Geology, University of Johannesburg P.O. Box 524, Auckland Park, 2006 South Africa

[6] Dept. of Earth and Atmospheric Sciences, Indiana University, Bloomington, IN 47408, USA [5] Earth and Environmental

[7] Division, Los Alamos National Laboratory, M.S. J535, P.O. Box 1663, Los Alamos, NM, 87545, USA

* Corresponding author:

Email: debarati.banerjee@student.nmt.edu

Ph: +1 575-405-4629

To be submitted to GCA, *for the Special Issue "Hydrothermal Geochemistry and Beyond: A*

Tribute to Terry M. Seward"

Keywords: Experimental geochemistry; Rare earth elements, Thermodynamics; Monazite solubility; Isotope dilution, Critical minerals.

ABSTRACT

A key aspect in the formation of rare earth elements (REE) deposits is the role of REE transport as aqueous REE complexes in supercritical hydrothermal solutions, where the nature of the aqueous complex is controlled by solution composition, temperature and pressure. Despite chloride being considered as one of the most abundant transporting ligands in magmatic-hydrothermal fluids, experimental investigations on the stability of aqueous REE chloride complexes are scarce above 300 °C. In this study, synthetic $NdPO_4$ crystals were reacted with non-saline and saline (0, 0.05 and 0.5 mNaCl), acidic (0.01 mHCl) aqueous solutions in a series of solubility experiments conducted at 500−700 °C and 1.7 kbar, where the solubilities were determined using a stable Nd isotope (^{145}Nd isotope spike) dilution technique. $NdPO_4$ solubility ranges between 28 ppm and 10,858 ppm, where solubility increases with both temperature and salinity. At 500 °C, log m$NdPO_4$ increases from -3.93 to -1.60 and there is a strong correlation between $NdPO_4$ solubility and NaCl concentrations (slope of 1.2 ±0.3), indicating stabilization of the Nd chloride aqueous complexes with a stoichiometry corresponding to $NdCl^{2+}$. At 600 °C, this correlation is weaker (slope of 0.4, log m$NdPO_4$ increases from -2.63 to -1.88) indicating the stabilization of both Nd chloride and hydroxyl species controlling solubility. At 700 °C, $NdPO_4$ solubility is largely independent of NaCl concentration indicating that solubility is controlled by Nd hydroxyl complexes, where stoichiometry suggests the neutral $Nd(OH)_3^0$ species is dominant. The solubility product (K_{sp}) of $NdPO_4$ is derived from experimental data with the relation: log K_{sp}=

-41.81 – 0.057T – 20987/T, with T temperature in Kelvin. Comparison of the measured Nd phosphate solubility to thermodynamic predictions using the available Helgeson-Kirkham-Flowers equation of state parameters for aqueous Nd complexes indicate that predictions are up to three orders of magnitude lower compared to experimental observations. This discrepancy is most pronounced in saline solutions, suggesting that thermodynamic properties of the REE chloride species in supercritical fluids require revision. Numerical simulations of fluid-rock interaction between acidic, saline fluids and a Strange Lake felsic mineral assemblage demonstrates that $NdPO_4$ solubility predictions from models are four to six orders of magnitude lower than those calculated based on empirical fits from experiments, which suggests that acidic, saline fluids may play an important role in mobilizing large amounts of light REE from 450 to 700 °C.

1. INTRODUCTION

The move of the energy sector towards green energy and the increase in demand for energy efficient devices has instigated a renewed interest in the rare earth elements (REE) (Balaram, 2019; Chakhmouradian and Wall, 2012; Goodenough et al., 2018). Neodymium is of particular importance for building strong permanent magnets in electric vehicles and wind turbines (Balaram, 2019; Chakhmouradian and Wall, 2012; Goodenough et al., 2018). Monazite is an important host mineral to Nd and other light (L)REE (La to Gd) in the Earth's crust (Balaram, 2019; Chakhmouradian and Wall, 2012; Harlov et al., 2016). Focus of monazite exploration and mining has expanded from placer deposits (e.g., the beach sand deposits in India; the paleo-placers of Witwatersrand in South Africa, river placers in Malaysia; Balaram, 2019) to include alkaline igneous complexes (e.g., Strange Lake deposit in Canada; Gysi et al., 2016), carbonatites (Bayan

Obo deposits, China; Fan et al., 2016; Mount Weld, Australia; Zhukova et al., 2021) and vein and skarn deposits (Bastnäs-type deposit, Sweden; Holtstam et al., 2014). Magmatic-hydrothermal REE deposits and the formation of monazite are commonly associated with hydrothermal activity (Banks et al., 1994; Dhote et al., 2021; Gysi et al., 2016; Harlov et al., 2016; Liu et al., 2019; Singh et al., 2018; Verplanck et al., 2022; Williams-Jones et al., 2000; Zhilong et al., 2007), which suggests that high temperature fluids play a critical role in REE fractionation, transport and deposition. Therefore, determining the temperatures, pressures and fluid compositions that facilitate REE mobilization is essential to understand the genesis of these REE deposits.

Thermodynamic modeling studies on fluid-rock reactions have shown that the formation of aqueous complexes plays a key role in REE mobilization (Migdisov et al., 2016; Pan et al., 2024; Perry and Gysi, 2018). Important REE complexing ligands include chloride, fluoride and sulfate anions for which robust thermodynamic data have been experimentally determined up to temperatures of ~300 °C (Migdisov et al., 2016). In many magmatic-hydrothermal REE deposits, chloride is one of the main ligands available for the formation of aqueous REE complexes as determined from fluid inclusion studies (Banks et al., 1994; Shu and Liu, 2019; Tillberg et al., 2019; Vasyukova et al., 2016; Vasyukova and Williams-Jones, 2018; Williams-Jones et al., 2000). To date, a few experimental studies have been conducted in supercritical aqueous fluids to identify the coordination of aqueous La, Nd, Eu, Gd, Yb, and Y chloride complexes (Guan et al., 2020, 2022; Liu et al., 2017; Louvel et al., 2015; Mayanovic et al., 2002, 2007, 2008, 2009; Schmidt et al., 2007). These studies generally show that addition of chloride and increased temperature result in the formation of stronger coordinated REE chloride complexes.

$NdPO_4$ solubility experiments have been conducted > 100 °C in a few studies including batch-type reactor experiments between 100 and 300 °C (Cetiner et al., 2005; Gysi et al., 2018; Poitrasson et al., 2004; Van Hoozen et al., 2020) and cold-seal pressure experiments between 300 and 800 °C and 2 kbar in the study by Pourtier et al. (2010). The studies of Poitrasson et al. (2004), Cetiner et al. (2005), and Van Hoozen et al. (2020) suggest that the Nd^{+3} species is predominant in acidic solutions of pH ~1 to 2 from 100 to 300 °C, and that $NdPO_4$ solubility is retrograde with increased temperature. Furthermore, the solubility experiments by Van Hoozen et al. (2020) and Gysi et al. (2018) indicate an increased importance of $REEOH^{2+}$ in acidic (pH=2) non-saline solutions >150 to 250 °C, which was confirmed in the comprehensive thermodynamic optimization study for the solubility of REE phosphates by Pan et al. (2024). However, the stability of the Nd^{3+} and Nd hydroxyl species versus the Nd chloride species at higher temperature is uncertain. Thermodynamic models generally suggest a predominance of the REE chloride complexes ($REECl^{2+}$ and $REECl_2^{+}$) in acidic (pH <2.5) saline aqueous solutions to ~300 °C (Migdisov et al., 2016). However, the stability of the $REECl_3^0$ species has been suggested to increase at higher temperature and has been identified in a few studies (e.g., Guan et al. 2020, 2022). Furthermore, the $NdPO_4$ solubility experiments by Pourtier et al. (2010) suggest that Nd hydroxyl complexes predominate at pH of 4 to 7.5 at 2 kbar between 300 and 800 °C.

To better understand the importance of Nd chloride and hydroxyl complexation in supercritical fluids, we conducted systematic $NdPO_4$ solubility experiments using cold-seal pressure vessels at 500 °C to 700 °C and 1.7 kbar in HCl-bearing solutions containing varying initial salinities (0–0.5 mNaCl). A stable ^{145}Nd isotope dilution technique was used to determine the Nd concentrations dissolved during the experiments. The $NdPO_4$ solubilities and reaction stoichiometries from experiments are compared with thermodynamic predictions based on the

113 available Helgeson-Kirkham-Flowers (HKF) equation of state parameters (Helgeson et al., 1981;
114 Shock and Helgeson, 1988; Tanger and Helgeson, 1988; Shock et al., 1992) for aqueous Nd species
115 and are used to derive the solubility product for monazite in supercritical fluids. The solubility
116 product is used to predict the Nd mobility in hydrothermal fluids as a function of cooling and fluid
117 to rock interaction, providing insights into the relevance of Nd mobility in ore forming systems.
118 Numerical simulations are performed between 450 – 700 °C equilibrating 1 kg of saline fluid (0.1-
119 1 mNaCl) with 1000g of pegmatite and tracking the solubility of monazite-Nd during cooling.

120

121 **2. MATERIALS AND METHODS**

122 *2.1. $NdPO_4$ synthesis and stock solution preparation*

123 The crystals used in the experiments are pure end member $NdPO_4$ crystals (Fig. 1A, B),
124 which were synthetically grown following the synthesis technique of Cherniak et al. (2004). At
125 first, a powdered hydrated Nd phosphate was precipitated from a 1:1 molar mixture of a $Nd(NO_3)_3$
126 solution and a $NH_4H_2PO_4$ solution, which was subsequently dried to a fine grained powder
127 consisting of $NdPO_4$. Approximately 0.9 grams of the finely powdered $NdPO_4$ precipitate was
128 then mixed with 25 grams of a Pb-free, 75/25 molar Na_2CO_3-MoO_3 flux. This mixture was then
129 packed into a Pt crucible which was the taken up to 1280 °C for 15 hours. The Pt crucible was
130 then cooled at 3 °C/h to 870 °C over a period of five days. The flux and the embedded $NdPO_4$
131 crystals were then boiled in distilled water until the crystals were freed from the flux. This process
132 required several washings until the flux was totally removed. The end result was inclusion free,
133 euhedral, pure $NdPO_4$ crystals with a natural distribution of Nd isotopes (Cherniak et al., 2004;

Gysi et al., 2018). This identical synthesis method has been used in previous REE phosphate solubility experiments (Gysi et al., 2015, 2018; Van Hoozen et al., 2020; Gysi and Harlov, 2021).

The starting experimental stock solutions include a non-saline (H_2O-HCl) solution and two saline (H_2O-HCl-NaCl) solutions spiked with a ^{145}Nd isotope. The Nd isotope spike solution was prepared by dissolving Nd_2O_3 (ISOFLEX, USA; certified 91.0 ± 0.4% ^{145}Nd enrichment) enriched in ^{145}Nd (Table 1) in pure HCl (trace metal grade, Fisher Scientific) to obtain an acidic solution. This solution was further diluted with MilliQ water (18 MΩ-cm) to obtain a final acidic (0.01 mHCl; pH 2 at room temperature) spike stock solution with 10.29 ± 0.02 ppm Nd. This solution was subsequently diluted with a 0.01 mHCl solution to prepare the experimental stock solutions and reach a starting Nd spike concentration of 0.249 to 0.264 ppm Nd (1-2% RSD, relative standard deviation; Table S1) (Table 2). The non-saline starting experimental stock solution was prepared by diluting a 0.1 mHCl standard solution (0.1001 ± 0.0005 mHCl, Inorganic Ventures) with MilliQ water and the Nd spike solution to reach a concentration of 0.01 mHCl and a pH of 2 at room temperature. The two saline starting experimental stock solutions with 0.05 and 0.5 mNaCl were prepared by dissolving NaCl powder (Alfa Aesar; 99.998% purity) in MilliQ water, followed by dilution with the 0.1 mHCl standard solution and the Nd spike solution to reach a final concentration of 0.01 mHCl and a pH of 2 at room temperature (Table S2).

2.1.2 Isotope dilution technique

We implemented the isotope dilution technique (Fig. 2) in our experiments following a method similar to that of Pourtier et al. (2010) to avoid the effects of precipitation of $NdPO_4$ upon

quenching on measured $NdPO_4$ solubility (Figs. 1E and F). The spiked experimental starting solutions have a $^{145}Nd/^{144}Nd$ ratio of 87.068 ± 0.005 and the $NdPO_4$ crystals have a natural isotopic $^{145}Nd/^{144}Nd$ ratio abundance of 0.348412 ± 0.000004. During the experiment, dissolution of the synthetic $NdPO_4$ crystals dilutes the $^{145}Nd/^{144}Nd$ isotopic ratio of the spiked solution, moving the $^{145}Nd/^{144}Nd$ isotopic ratio towards the composition of the $NdPO_4$ crystal (Fig. 2). The $^{145}Nd/^{144}Nd$ ratio of the experimental fluid (i.e., from mixing of Nd from the crystal with the Nd in the solution from spike) remains unchanged following quenching even if $NdPO_4$ precipitates, because isotopic fractionation does not occur for heavy isotopes (Pourtier et al., 2010). The $^{145}Nd/^{144}Nd$ isotopic ratio in the solution can therefore be defined by the equation of binary isotopic mixing and provide a record of the mass of $NdPO_4$ dissolution that occurred at the run conditions ($^{Total}Nd_{NdPO_4}$) according to:

$$ {}^{Total}Nd_{NdPO_4} = {}^{Total}Nd_{spike} \times \frac{X_{spike}^{145Nd} - \left[\left(\frac{^{145}Nd}{^{144}Nd}\right)_{sol} \times X_{spike}^{144Nd}\right]}{\left[\left(\frac{^{145}Nd}{^{144}Nd}\right)_{sol} \times X_{NdPO_4}^{144Nd}\right] - X_{NdPO_4}^{145Nd}} \quad \text{(Eq. 1)} $$

where X_{spike}^{145Nd} is the isotopic abundance of ^{145}Nd in the spike (91.2% ± 0.2), X_{spike}^{144Nd} is the isotopic abundance of ^{144}Nd in the spike (1.047 ± 0.002), $X_{NdPO_4}^{145Nd}$ and $X_{NdPO_4}^{144Nd}$ are the isotopic abundances of ^{145}Nd and ^{144}Nd in the $NdPO_4$ crystal (8.29 ± 1.2 and 23.7 ± 1.9) that is dissolved during the experiment (Table 1). The ratio $\left(\frac{^{145}Nd}{^{144}Nd}\right)_{sol}$ is the final ratio of $^{145}Nd/^{144}Nd$ that was measured in the quenched experimental solutions using multi-collector inductively coupled plasma mass spectrometry (MC-ICP-MS). The variable $^{Total}Nd_{spike}$ corresponds to dissolved Nd concentration (mol/kg) in the solution contributed by the spike, which was determined by solution ICP-MS and

175 variable $^{Total}Nd_{NdPO_4}$ corresponds to the unknown total concentration of dissolved Nd in solution
176 at temperature and pressure contributed from the dissolved $NdPO_4$ only. The relative standard
177 deviation (RSD, 2σ error) reported in Table 2 was calculated by propagating the relative analytical
178 uncertainty of each variable in Eq. 1. The experimental uncertainty is calculated by duplicate
179 experiments and is 44%, which is used in all figures.

180

181 *2.2. Experimental method*

182 Solubility experiments were conducted in gold capsules containing each a synthetic $NdPO_4$
183 crystal and the ^{145}Nd isotope spiked starting experimental solutions (Table 2), which were
184 equilibrated for 96 to 144 h in Waspaloy (Ni based super alloy) pressure vessels at 500, 600, and
185 700 °C and 1.7 kbar. The gold capsules are created from 25–30 mm lengths of 4 mm outer diameter
186 (3.75 mm internal diameter) gold tubing. First, gold tubing is cut to size and soaked in 9% nitric
187 acid for 24 hours, then the tubes are soaked in MilliQ water for another 24 h and dried over flame.
188 Once dried, one end of the gold capsule is tri-crimped and welded shut with precision welding
189 using a Lampert PUK 5.1 welding system. Each gold capsule is loaded with a $NdPO_4$ crystal and
190 a known mass of experimental stock solution (Table 2) and welded closed. The masses of the
191 crystal and solution components are measured during each step of the capsule loading process.
192 When loaded capsules are closed, the welds are completed at slow rate in order to avoid heating
193 up the capsule, which can lead to solution volatilization. The closed capsules are weighed, then
194 heated on a hotplate (100–125 °C) to check for any leaks in welds. Capsules that lost mass during
195 the hot plate tests were discarded and not used in this study.

196 Following assembly and heat tests, capsules are placed into the hotspots of Waspaloy (Ni
197 based super alloy) pressure vessels, followed by H_2O (the pressurizing medium) and a Ni-filler
198 rod, which exerts an intrinsic fO_2 that is close to the Ni-NiO buffer on the capsule assembly
199 (Venezky & Rutherford, 1999). Vessels are sealed and pressurized to 2.0 to 2.3 kbar at room
200 temperature for a span of 24 hours to ensure seals will hold at the target pressure (1.7 kbar)
201 throughout the run duration. Vessels are placed in Thermo Scientific Lindberg Blue horizontal
202 tube furnaces and are heated to the target run temperature. The experimental temperatures are
203 monitored by external thermocouples (K-type thermocouples, Ni-Cr/Ni) inserted into a borehole
204 that is adjacent to the hotspot of the vessel, as well as an internal thermocouple within the
205 horizontal furnaces. Comparison of the temperature measured by the external thermocouple with
206 the actual temperature of the hotspot of the vessels suggests that the external thermocouple reads
207 within ± 6 °C of the hotspot temperature. The experimental condition was reached and stabilized
208 within 90 minutes of start and was maintained for equilibration for 96 to 168 h.

209 On completion of the equilibration time, the experiments are quenched isobarically to
210 minimize $NdPO_4$ re-precipitation and to prevent capsule rupture. Vessels are removed from the
211 horizontal furnace and plunged into a volume of water (at room temperature); this quenching
212 method typically cools an experiment in ~30–60 seconds (Waters et al. 2015). Following
213 quenching and extraction from the vessels, capsules are weighed to monitor for mass loss. Only
214 capsules that did not suffer any mass loss during equilibration and quenching, were considered and
215 included in this study. The capsules are taken out of the vessels, weighed, and a section of the
216 capsule wall is punctured close to the tricrimp weld to prevent crushing of any crystalline products
217 (Fig. S3). The capsules were soaked in 20 ml of 2% nitric acid for 20 minutes to promote solution

exchange. Following sonication and extraction of the reacted solution, the capsules are carefully peeled opened to completely expose the inner walls of the capsule along with the crystalline mass (Fig. S3). The crystalline mass is extracted as much as possible and weighed. The crystals and capsule materials are later examined for precipitation and evidence of dissolution using a scanning electron microscope (SEM).

2.3. Analytical Methods

Unreacted and reacted $NdPO_4$ crystals were studied using a binocular microscope and a JEOL JSM-IT700HR Field Emission Scanning Electron Microscope (FE-SEM). The crystals were analyzed without carbon coating, using an acceleration voltage of 2 kV and at a working distance of 10 mm (Fig. 1).

The Na concentrations of the starting experimental stock solutions (Table 2) were analyzed using an Agilent 5900 inductively coupled plasma optical emission spectroscopy (ICP-OES) instrument at the analytical chemistry laboratory at the New Mexico Bureau of Geology and Mineral Resources, New Mexico Institute of Mining and Technology. Samples were prepared by dilution with a 2% nitric acid (trace metal grade, Fisher Scientific) blank. Single element Na standard solution (Inorganic Ventures, CGNA1, 1002 ± 4µg/ml Na) was used for calibration and diluted with a 2% nitric acid matrix. The analytical reproducibility of Na measurements is better than 3% in the measured concentration range of 0.2 to 50 ppm.

The Nd spike concentrations (Table 2) were determined using an Agilent 7500 quadrupole solution ICP-MS instrument at the analytical chemistry laboratory at New Mexico Bureau of Geology and Mineral Resources. External calibration standards were prepared from a single

element Nd standard (Inorganic Ventures, CGND1, 1000 ± 3 μg/ml Nd), diluted to various concentrations (0.5 ppt – 14.2 ppb) in 2% nitric acid matrix (trace metal grade, 70%, Fisher Scientific). The analytical reproducibility on the measured Nd is better than 2%. The instrument drift correction was performed using an In-Ir in-line internal standard solution (50 ppb In and 20 ppb Ir, SCP Science).

Isotopic Nd ratios were measured in the quenched experimental solutions using a Thermo Scientific Neptune MC-ICP-MS, at the Johnson mass spectrometer laboratory at New Mexico State University. Before analysis, each Faraday cup is calibrated by peak centering on each of the isotopic masses of Nd's seven isotopes (^{142}Nd, ^{143}Nd, ^{144}Nd, ^{145}Nd, ^{146}Nd, ^{148}Nd, ^{150}Nd). After calibration, each Faraday cup measures specific elemental mass to charge ratios, which in turn is used to evaluate the isotopic ratio of the dissolved Nd (Lin et al., 2016). The internal standard used for the instrument calibration is JNdi-1 standard from Geological Survey of Japan (Tanaka et al., 2000). After each sample run, the solution nebulizer is rinsed in 2% nitric acid blank to achieve base line (which is defined as the signal intensity from 2% nitric acid blank). The internal standard is analyzed before and after sample analysis. The analytical precision associated with the isotopic ratios of ^{145}Nd/^{144}Nd vary from 0.002% to 0.2% depending on the concentration. Measured isotopic composition and analytical uncertainty are reported in Table 1 for the experimental starting stock solutions and in Table 2 for reacted experimental solutions.

2.4. Data treatment

Speciation, pH, and ion activity calculations are performed in the Na-Nd-P-Cl-O-H system using the GEMS code package v.3.7 (Kulik et al., 2013; https://gems.web.psi.ch/), the TSolMod library (Wagner et al., 2012), and the MINES thermodynamic database (Gysi et al., 2023; https://geoinfo.nmt.edu/mines-tdb/). The thermodynamic properties of the aqueous species were calculated using the revised HKF equation-of-state (Helgeson et al., 1981; Shock et al., 1992; Shock & Helgeson, 1988; Tanger & Helgeson, 1988). The properties of water were taken from the IAPS-84 equations-of-state (Kestin et al., 1984).

Thermodynamic data for major aqueous P-species ($H_3PO_4^0$, $H_2PO_4^-$, HPO_4^{2-}, and PO_4^{3-}, $H_2P_2O_7^{-2}$ and $HP_2O_7^{-3}$), Nd hydroxyl complexes ($NdOH^{2+}$, $Nd(OH)_2^+$, $Nd(OH)_3^0$, and, Cl^-, OH^-, H^+ were taken from SUPCRT92-slop98.dat (Johnson et al., 1992). These data were derived by Shock and Helgeson (1988), Shock et al. (1989, 1997), and Haas et al. (1995), hereafter referred to Supcrt92. The properties of the Nd^{3+} aqua ion are updated based on the REE phosphate thermodynamic optimization study by Pan et al. (2024). Thermodynamic data and HKF parameters that were updated based on high temperature experimental work include: HCl^0 from Tagirov et al. (1997); Nd chloride species ($NdCl^{2+}$, $NdCl_2^+$) measured up to 300 °C by Migdisov et al. (2009, 2016); Na-species ($NaCl^0$, Na^+, $NaOH^0$) and K-species (KCl^0, KOH^0) optimized by Miron et al. (2016) using GEMSFITS (Miron et al., 2015). Thermodynamic data for solids include: halite from Robie and Hemingway (1995); $NdPO_4$ from Ushakov et al. (2001), Thiriet et al. (2005), Popa and Konings, (2006); Nd oxides and hydroxides from Diakonov et al. (1998), Konings et al. (2014), and the compilation of Navrotsky et al. (2015). The Gibbs energy of formation of all species in the Nd-PO_4-HCl-NaCl-H_2O system are provided in Table S4 along with the references used in calculations.

The activities of aqueous species were calculated at the experimental temperature and pressure from the measured NaCl and HCl concentrations (via ICP-MS) in the experimental starting stock solutions, and the Nd and P concentrations, measured in the quenched experimental solutions (via MC-ICP-MS). The equilibrium pH is calculated in GEMS at each experimental temperature and pressure from the Gibbs energy minimization and the calculated chemical potentials of all species within the Nd-PO_4-HCl-NaCl-H_2O system. Full details about the GEMS3K chemical solver algorithm are provided in Kulik et al. (2006, 2013).

The extended Debye-Hückel equation (Robinson and Stokes, 2002) was used to calculate the activity coefficients (γ_i) of charged species (e.g., Nd^{3+}) according to,

$$\log\gamma_i = \frac{-Az_i^2\sqrt{I}}{1+\mathring{a}B\sqrt{I}} + \Gamma_\gamma + b_\gamma I \qquad \text{(Eq. 2)}$$

where I is the effective ionic strength given by,

$$I = \left(\frac{1}{2}\right)\Sigma_i m_i z_i^2 \qquad \text{(Eq. 3)}$$

A and B are the Debye-Hückel parameters (Helgeson and Kirkham, 1974; Helgeson et al., 1981); $\mathring{a}$ is the ion size parameter (i.e., the model assumes a common value of 3.72 Å for NaCl) and b_γ is the temperature and pressure dependent extended term parameter, which are both consistent with the NaCl background electrolyte model (Helgeson et al., 1981; Oelkers and Helgeson, 1990); m_i is the molal concentration of charged species, and z_i is the charge of the i^{th} aqueous species; Γ_γ is the mole fraction to molality conversion factor. The activity of water is calculated form the osmotic coefficient (Helgeson et al., 1981). Because the experimental solutions are prepared with low

concentrations of NaCl and HCl (Table 2), the overall ionic strength is relatively low and reduces the uncertainties in the calculated activity coefficient of the charged species.

The solubility product or reaction quotient ($Q_{sp} = a\mathrm{Nd}^{+3} \times a\mathrm{PO_4}^{-3}$) of $NdPO_4$ is calculated from the activities of Nd^{+3} and PO_4^{-3} retrieved for each experimental solution from the speciation calculations at temperature and pressure using GEMS, according to the reaction,

$$NdPO_4\,(s) = Nd^{+3} + PO_4^{-3}\ (K_{sp} \text{ or } Q_{sp}) \qquad \text{(Eq. 4)}$$

The equilibrium constants (K_{sp}) for this reaction are calculated at each temperature and pressure using the standard Gibbs energies from thermodynamic tables (Table S4). The $NdPO_4$ saturation indices (*SI*) are then calculated at each experimental condition according to:

$$SI = \log\left(\frac{Q_{sp}}{K_{sp}}\right) \qquad \text{(Eq. 5)}$$

Large deviations of *SI* values from 0 were assumed to indicate that the thermodynamic properties for aqueous species need to be revised over the range of temperature in this study. We use our experiments to update these K_{sp} values, where we assume that $Q_{sp}=K_{sp}$ at $NdPO_4$ saturation. Note that Eq. 4 is chosen to allow comparison with other solubility studies, but in GEMS one could also calculate the reaction quotient using the major species present at given pH (e.g., $H_3PO_4^0$ at acidic conditions) and combine them with phosphoric acid dissociation constants calculated from thermodynamic tables. However, the results will be the same and constrained by internal consistency of the thermodynamic database and full speciation calculations using GEMS (see also Gysi et al., 2015, 2018).

3. EXPERIMENTAL RESULTS

3.1. Experimental replicates and assessment of experimental uncertainty

Three experiments were conducted at 500 °C, 1.7 kbar and 0.01 mHCl with durations of 96 h and 168 h. The replicate experiments at 96 h were used to assess the uncertainty while the experiments with variable equilibration durations were performed to confirm steady-state conditions between the $NdPO_4$ crystal and the solutions.

The solubility of $NdPO_4$ reported in Table 2 is expressed as the logarithmic value of the molality of dissolved $NdPO_4$ (log $mNdPO_4$) without the Nd isotopic spike. The values of log $mNdPO_4$ are -3.93 (28.2 ppm) and -3.50 (74.9 ppm) for experiments with a duration of 96 h, respectively and -3.61 (59 ppm) for the experiment with a duration of 168 h (Table 2; Figure S5). Based on these measured solubilities, it appears that a steady state is attained in the experiments within 96 h. The average solubility at 500 °C in the non-saline fluid is 54 ± 24 ppm, which corresponds to an experimental uncertainty of 44%; we apply this uncertainty to all experiments. The experimental uncertainty is propagated through the geochemical simulations and on all of the figures that use experimentally derived $NdPO_4$ solubility. These results are consistent with Pourtier et al. (2010), who observed no significant changes in the measured solubility of $NdPO_4$ at temperatures as low as 300 °C between durations of 96 h and 15 days of durations using fluid compositions similar to this study.

3.2. $NdPO_4$ reaction textures

Unreacted and reacted crystals and the gold capsule after extraction of solution and run products were analyzed using a binocular microscope and FE-SEM (Fig. 1). The unreacted $NdPO_4$ crystal has well-defined crystal surfaces and sharp edges showing a monoclinic structure (Figs. 1A and B). Some of the crystals became brittle and broke into pieces upon opening the gold capsules after experiments (Fig. 1C). The morphology of the reacted crystals at 500 °C and 1.7 kbar indicates the development of dissolution textures (i.e., rounded crystals edges with the formation of etch pits on crystal surfaces; Fig. 1D). An image of the inner walls of a gold cell and $NdPO_4$ crystal surface under SEM indicate significant re-precipitation of $NdPO_4$ upon quenching (Figs. 1E and F); the Nd and P composition and stoichiometry of the secondary precipitates were confirmed using SEM-EDS analyses.

3.3. $NdPO_4$ solubility as a function of temperature and salinity

Nd concentrations vary as a function of both temperature and salinity (Fig. 3). A comparison between the solubility of $NdPO_4$ in non-saline and saline (0.05 and 0.5 mNaCl) experimental solutions as a function of temperature is shown in Figure 3A. In the non-saline experiments, the log $mNdPO_4$ values increase from -3.93 (28 ppm $NdPO_4$) at 500 °C to -2.11 (1,875 ppm $NdPO_4$) at 700 °C. In the saline experiments with 0.05 mNaCl, the log $mNdPO_4$ values increase from -2.61 (585 ppm $NdPO_4$) at 500 °C to -1.34 (10,858 ppm $NdPO_4$) at 700 °C; the latter is the highest recorded log $mNdPO_4$ value in this study. In the saline experiments with 0.5 mNaCl, the solubility trend for $NdPO_4$ becomes reversed (i.e., retrograde) with log $mNdPO_4$ values decreasing from -1.60 (6,000 ppm $NdPO_4$) to -2.36 (1,040 ppm $NdPO_4$) from 500 to 700 °C.

The salinity of the solutions exerts a strong control on $NdPO_4$ solubility in the experiments as temperature increases from 500 °C to 700 °C (Fig. 3B). At 500 °C, the log $mNdPO_4$ values increase from -3.93 (28 ppm $NdPO_4$) to -1.60 (6,000 ppm $NdPO_4$) with increasing NaCl concentrations from 0 to 0.5 mNaCl. At 600 °C, the log $mNdPO_4$ concentrations are higher in the lower salinity range and increase from -2.63 (557 ppm $NdPO_4$) to -1.88 (3,169 ppm $NdPO_4$) as NaCl concentrations increase from 0 to 0.5 mNaCl. At 700 °C, the log $mNdPO_4$ values are significantly higher in the at low salinity where they increase from -2.11 (1,875 ppm $NdPO_4$) to -1.34 (10,858 ppm $NdPO_4$) at NaCl concentrations from 0 to 0.05 mNaCl. In contrast, the log $mNdPO_4$ values subsequently decrease from -1.34 (10,858 ppm $NdPO_4$) to -2.36 (1,040 ppm $NdPO_4$) at 700 °C as NaCl concentrations increase from 0.05 to 0.5 mNaCl.

The linear relationship of log $mNdPO_4$ and the concentration of NaCl (m_{NaCl}) can be defined empirically:

$$\log mNdPO_4 = m(m_{NaCl}) + b \quad \text{(Eq. 6)}$$

where m and b are the slope and intercept for each isotherm at 1.7 kbar (Fig. 3B). The resulting fits yield: m = 3.89 (±0.91) and b = -3.48 (±0.27) at 500 °C, m= 1.33 (±0.91) and b= -2.53 (±0.27) at 600 °C; m=-1.20 (±0.92) and b= -1.72 (±0.27) at 700 °C, where errors (±1σ) are determined using experimental uncertainty and Monte-Carlo regression. The temperature dependence of the slope term and the intercept between 500 and 700 °C and 1.7 kbar (Fig. 3C) is given by

$$m = -0.03T + 16.61 \quad \text{(Eq. 7)}$$

$$b = 0.01T - 7.86 \quad \text{(Eq. 8)}$$

382

383 **4. DISCUSSION**

384 *4.1. Nd speciation as a function of chlorinity and pH*

385 The solubility of $NdPO_4$ not only depends strongly on temperature but also the salinity and
386 the calculated pH of the experimental solutions, both affecting Nd speciation (Table 3). The Nd
387 species that control solubility in the experiments can be derived from the stoichiometric
388 relationship by combining the $NdPO_4$ solubility reaction (Eq. 4) with aqueous speciation reactions
389 including Nd chloride, Nd hydroxyl, and phosphate species:

390 $$NdPO_4 + 2Cl^- + 3H^+ \rightleftharpoons NdCl_2^+ + H_3PO_4^0 \quad \text{(Eq. 9)}$$

391 $$NdPO_4 + Cl^- + 3H^+ \rightleftharpoons NdCl^{2+} + H_3PO_4^0 \quad \text{(Eq. 10)}$$

392 $$NdPO_{4(s)} + 3H^+ \rightleftharpoons Nd^{3+} + H_3PO_4^0 \quad \text{(Eq. 11)}$$

393 $$NdPO_{4(s)} + H_2O_l + 2H^+ \rightleftharpoons Nd(OH)^{+2} + H_3PO_4^0 \quad \text{(Eq. 12)}$$

394 $$NdPO_{4(s)} + 2H_2O_l + H^+ \rightleftharpoons Nd(OH)_2^+ + H_3PO_4^0 \quad \text{(Eq. 13)}$$

395 $$NdPO_{4(s)} + 3H_2O_l \rightleftharpoons Nd(OH)_3^0 + H_3PO_4^0 \quad \text{(Eq. 14)}$$

396 $$NdPO_{4(s)} + 3H_2O_l \rightleftharpoons Nd(OH)_3^0 + H_2PO_4^- + H^+ \quad \text{(Eq. 15)}$$

397 $$2NdPO_{4(s)} + 5H_2O_l \rightleftharpoons 2Nd(OH)_3^0 + H_2P_2O_7^{-2} + 2H^+ \quad \text{(Eq. 16)}$$

398 The slope relationships determined by linear regression of log $mNdPO_4$ and log mCl or pH
399 (Fig. 4) correspond to an average stoichiometry controlled by one or several reactions in Eqs. 9-

16 above. Correlations between log $mNdPO_4$ and log mCl that yield a slope of 2 indicate $NdCl_2^+$ dominance (Eq. 9), a slope of 1 indicate $NdCl^{+2}$ (Eq. 10), and a slope of 0 indicates Nd^{3+} (Eq. 11) and all hydroxyl species (i.e., because the reactions are independent of Cl activity). Correlations between log $mNdPO_4$ and pH that yield a slope of -3 indicates predominance of Nd^{3+} (Eq. 11) or Nd chloride species, a slope of -2 indicates $Nd(OH)^{+2}$ (Eq. 12), a slope of -1 indicates $Nd(OH)_2^+$ (Eq. 13), and a slope of 0 indicates $Nd(OH)_3^0$ (Eq. 14). Finally, a positive slope of 1 is expected if Nd^{3+} is complexed with either $H_2PO_3^-$ or the polyphosphate $H_2P_2O_7^{-2}$ species (Eqs. 14-16).

At 500 °C, the regressed slope between log $mNdPO_4$ vs. log mCl corresponds to an average stoichiometry of 1.24 (± 0.29) indicating that the $NdCl^{+2}$ species predominates with subordinate $NdCl_2^+$ (Fig. 4A; Eqs. 9-10). At 600 °C, the slope decreases to 0.45 (± 0.29) indicating a combination of $NdCl^{2+}$ and Nd hydroxyl species control $NdPO_4$ solubility (Fig. 4C). At 700 °C, $NdPO_4$ solubility is independent of log mCl concentrations with a slope close to 0 (Fig. 4E), indicating that Nd hydroxyl species control $NdPO_4$ solubility. The average Cl stoichiometry derived from the linear regressions above can be subtracted from log $mNdPO_4$ to assess the stability of subordinate Nd hydroxyl species as a function of pH (Fig. 4B, D). Corrected log $mNdPO_4$ are independent of pH at 500 and 600 °C, which indicates that the neutral $Nd(OH)_3^0$ species is the predominant hydroxyl species in these experiments (Fig. 4B, D).

The pH values are calculated using GEMS at temperature and pressure for each experimental solution (Table 3). In the 700 °C experiments, the trend in log $mNdPO_4$ with pH is ambiguous when calculated pH values exceed 6.7 (Fig. 4F). Speciation calculations at 700 °C predict stabilization of polyphosphate species ($H_2P_2O_7^{-2}$ and $HP_2O_7^{-3}$; Table 3). The predicted predominance of polyphosphate species at >600 °C and pH >5 has previously been described in

422 Pourtier et al. (2010). However, the accuracy in extrapolating the thermodynamic properties of
423 these polyphosphate aqueous species using the HKF equation of state parameters from Shock and
424 Helgeson (1988) and Shock et al. (1989, 1997) is unknown at high temperatures. Therefore, to be
425 conservative in our interpretation of these data, we report speciation data for the 700 °C
426 experiments in Table 3, but do not use the calculated pH to derive species stoichiometry of Nd
427 hydroxyl species.

428

429 *4.2. Speciation and Nd mineral saturation index calculations*

430 The Nd species stoichiometry derived from linear regression (Figure 4) generally agree
431 with the calculated species activities (Table 3; Fig. 5). Figure 5 shows the activity of Nd^{3+} is low
432 (Fig. 5A) and that $NdCl^{+2}$ species control $NdPO_4$ solubility in the low pH range (~2 to 5.5; Fig
433 5B). Increased stabilization of the $Nd(OH)_2^+$ (Fig. 5E) and $Nd(OH)_3^0$ (Fig. 5F) species occurs at
434 high pH (~5.5 to 7). The properties for REE chloride and HKF equation of state parameters derived
435 by Migdisov et al. (2009) are based on experimental data collected up to ~300 °C, and therefore
436 the extrapolations to calculate speciation at temperatures of 500 to 700 °C have a high uncertainty
437 in their accuracy. This is reflected, for example, in the calculated saturation indices (*SI*) for $NdPO_4$
438 described below. Similarly, the thermodynamic properties derived by Haas et al. (1995) for the
439 REE hydroxyl complexes and the HKF equation of state parameters generated in their study are
440 based on low temperature experiments (generally <100 °C). Hence, the following discussion on
441 Nd speciation in the experiments describes the overall speciation trends of the experimental
442 solutions as a means to interpret the Nd solubility results, but their accuracy is uncertain.

443 The $NdCl^{2+}$ species is predicted to be the most stable Nd chloride species in the
444 experimental solutions (Table 3, Fig. 5B), which is consistent with the stoichiometry determined
445 from linear regression in Figure 4. At 500 °C, increasing salinity from 0 to 0.5 mNaCl results in a
446 pH increase from 2.5 to 6.1 and concomitantly increases the stability of both the $NdCl^{2+}$ and
447 $NdCl_2^+$ species (Fig. 5A, C). In contrast, experiments conducted at 600 °C display a slight decrease
448 in the calculated $NdCl^{2+}$ species activity with increased NaCl concentration due to increased pH
449 values from 4.2 to 6.7 and stabilization of the Nd hydroxyl complexes (Fig. 5C), which is
450 consistent with reaction stoichiometry (Fig. 4).

451 Another factor to consider is the potential saturation of secondary REE solid phases that
452 could affect the precipitation of Nd in the experiments (Table 4). Figure 6 shows a summary of
453 calculated pH values (Table 3) and saturation indices for Nd phosphate, hydroxide and oxide as a
454 function of NaCl concentrations (Table 4). The precipitation of other REE phases either upon
455 saturation at the experimental temperature or quenching does not affect the calculated dissolved
456 $NdPO_4$ because the isotope dilution method is used. Therefore, the Nd isotopic composition only
457 depends on how much Nd dissolved from the $NdPO_4$ and not on the amounts of precipitated solids.
458 The calculated pH of the experimental solutions reaches values ≥2.5 with increased temperature
459 and salinity (Fig. 6A). The REE solid saturation indices (Figs. 6 B-D; Eqs. 4 and 5) indicate that
460 $NdPO_4$ is oversaturated in all of the experiments, whereas Nd hydroxide and oxide are predicted
461 to be undersaturated at low salinities and at a temperature of 500 °C. At 600 °C and NaCl
462 concentrations of 0.05 to 0.5 mol/kg, Nd hydroxide and oxide are predicted to be close to saturation
463 or oversaturated. While the speciation calculations result in the supersaturation of these minerals,

464 a saturation index reaching 12 (i.e., experiment EF1-7, Table 4) for $NdPO_4$ indicates a problem
465 with the thermodynamic properties for the Nd compounds.

466

467 *4.2. Comparison to previous $NdPO_4$ solubility studies: implications for the thermodynamic*
468 *properties of REE aqueous complexes in supercritical fluids*

469 Figure 7 shows a comparison between $NdPO_4$ solubility values determined in experiments
470 from the literature (Table 5) and modeling predictions as a function of temperature between 100
471 and 800 °C. Overall, the experimentally derived data for $NdPO_4$ solubility display an increase of
472 ~6-6.5 orders of magnitude from 100 to 800 °C. This corresponds to a concentration range of 1.6
473 ppb (10^{-3} ppm) to 0.2 ppm $NdPO_4$ (log $mNdPO_4$ = -8.2 to -6) at temperatures between 100 and
474 300 °C at the saturated water vapor pressure, and concentrations ranging from 0.5 to 644 ppm
475 $NdPO_4$ (log $mNdPO_4$ = -5.7 to -2.6) at temperatures between 300 and 800 °C at higher pressures.
476 Differences between the log $mNdPO_4$ values from this study and Pourtier et al. (2010), who also
477 conducted experiments at temperatures ≥500°C, are due to differences in experimental pH, ionic
478 strength, chlorinity and the stabilized Nd-ligand (i.e., Nd^{3+} aqua ion, Nd chloride, Nd hydroxyl).
479 Additional variations between experimental studies are often due to addition of phosphorus in the
480 lower temperature experiments (Table 5), which reduces the $NdPO_4$ solubility considerably.
481 Nevertheless, despite their broad pH range, the overall trend shown in Figure 8 clearly indicates
482 large discrepancies between the modeled $NdPO_4$ solubility versus the experimentally measured
483 values. These discrepancies become very large at temperatures above 400 °C.

Experimental conditions and methods of this study are similar to experiments conducted by Pourtier et al. (2010), who investigated $NdPO_4$ solubility as a function of pH and chlorinity in H_2O–NaCl ± HCl ± NaOH fluids at 350-800 °C and 2–5 kbar. The $NdPO_4$ solubility is 1 – 3 orders of magnitude higher at a given temperature in Cl-rich fluids in this study compared to the solubility in Cl-poor fluids in Pourtier et al. (2010) (e.g., Fig. 8). Thus, differences in $NdPO_4$ solubility arise from compositional variation in experimental fluids between these studies. Pourtier et al. (2010) used H_2O in isotope dilution experiments from 350-800°C, whereas our experiments were conducted in HCl ± NaCl fluids. Pourtier et al. (2010) also reports $NdPO_4$ solubility results determined by mass loss at 650°C for six HCl and NaCl-bearing experiments, which overlap with our dataset (log $mNdPO_4$ ranges from -3.21 to 2.37; Table S6). In this study the $NdCl^{2+}$ species is predominant at 500 °C (Fig. 5B), that activity of $NdCl^{2+}$ is similar to $Nd(OH)_3^0$ (Fig. 5F) at 600 °C and $Nd(OH)_3^0$ indicated to predominate at 700 °C (Figure 5; Figure S5). At lower chlorinity in Pourtier et al. (2010), the $Nd(OH)_3^0$ is the dominant species in all experiments.

Experimental data from Pourtier et al. (2010) were assessed using GEMS to model the variations in pH and predicted speciation and compare to results from this study (Table S6). The pH values predicted using GEMS for experimental solutions in Pourtier et al. (2010) agree within ≤0.2 log units with their calculations. Calculated pH values at temperatures ≥450 °C in this study (see Table S6 and Pourtier et al., 2010, their Table 2) are systematically higher than those reported in Pourtier et al. (2010). This discrepancy is likely due to our use of the updated thermodynamic data for Na^+ and $NaOH^0$ from Miron et al. (2016). The Nd chloride and Nd hydroxyl species predicted in this study and those reported in Pourtier et al. (2010) are similar (Table 5; Table S6). The $Nd(OH)_2^+$ and $Nd(OH)_3^0$ predominate speciation at pH of 4 – 5 at 350 to 800 °C and $Nd(OH)_3^0$

predominates at pH of >5.8 in experiments from Pourtier et al. (2010). The $NdCl^{+2}$ species is predominant in most experiments where mCl > mNa (Table S6), which is consistent with results from this study where mCl is always larger than mNa. For experiments where mNa > mCl, the dominant phosphate species in experiments from Pourtier et al. (2010) varies between $H_2PO_4^-$ or $H_3PO_4^0$, similar to our results (Table 3). We also find that the activity of the polyphosphate species, $H_2P_2O_7^{-2}$, is elevated ($10^{-4.8}$ to $10^{-3.6}$; Table S6) and comparable to either $H_2PO_4^-$ or $H_3PO_4^0$ in experiments that have been buffered with phosphoric acid or where log $mNdPO_4$ > -3.8. Differences in speciation calculations between this study and Pourtier et al. (2010) results mostly from updated thermodynamic properties for Nd chloride species, which are based on Migdisov et al. (2009) in this study.

Finally, the predicted solubility of $NdPO_4$ (Eq. 4; Figure 7) depends on the updated thermodynamic properties of $NdPO_4$ (Ushakov et al. (2001), Thiriet et al. (2005), Popa and Konings, (2006), Nd^{3+} (updated to 300 °C in Pan et al., 2024), Nd chloride complexes (updated to 300 °C in Migdisov et al., 2009) and hydroxyl complexes (Haas et al., 1995) which have been extrapolated to the high temperatures used in this study. The Nd chloride species were updated based on experimental data (Migdisov et al., 2009) and generally show a good reproducibility between the NaCl- and HCl-bearing experiments up to ~350 °C. Above this temperature it is apparent that modeled predictions no longer reproduce the experimentally measured Nd solubility, therefore it is important that the Nd chloride species need to be updated taking into consideration high temperature experimental data. Similarly, the prediction of Nd hydroxyl species relevant for experiments at higher pH values such as experiments conducted at pH of 5 to 7 (Gibert and Montel, 1996) also rely on extrapolations of low temperature thermodynamic data from Haas et al. (1995).

These extrapolations do not reproduce experimentally measured solubilities at high temperature and therefore need to be revised.

4.3. Derivation of the solubility product ($logQ_{sp}$) and effects of temperature on $NdPO_4$ solubility

The solubility data of the studies listed in Table 5 were used to recalculate the solubility product of $NdPO_4$ according to Eq. 4 as a function of pressure and temperature. While the calculated activity of Nd^{3+} (Table 3) will depend on the stability of the chloride and hydroxyl species (Eqs. 9-16), we assume here that the calculated activities of Nd^{3+} and PO_4^{3-} can be used as a first approximation to determine the equilibrium constant Q_{sp} (assumption $Q_{sp} = K_{sp}$) of the $NdPO_4$ dissolution reaction in the experimental solutions (Fig. 8). Monazite solubility experiments have been grouped together into $\log Q_{sp}$ values derived at P_{sat} (VanHoozen et al., 2020; Cetiner et al. 2005; Poitrasson et al., 2004) and between 1.7 to 2 kbar (this study; Pourtier et al., 2010; Gilbert and Montel, 1996) to compare them to our experimental data (Table 6). Note that other REE phosphate solubility experiments by Tanis et al. (2012) and Ayers and Watson (1991) indicate that pressure has a minimal effect on the solubility of REE phosphate.

The $\log Q_{sp}$ values (Fig. 8) determined for experiments ≥ 300 to 800 °C can display relatively large variations due to the broad pH range and chemistry of the solutions used in these experiments (Table 5). Nevertheless, a fit through the experimental solubility data indicates clear trends when comparing the solubility curves at P_{sat} and elevated pressure (Fig. 8). Overall, $NdPO_4$ displays a retrograde solubility product (Eq. 4) with increasing temperature at both sub- and supercritical temperatures; solubility in supercritical fluids is however higher at given temperature

549 than at subcritical conditions. In contrast to the predicted solubility products, the measured
550 experimental solubility data suggest a prograde solubility displaying an overall increase of log
551 m$NdPO_4$ concentrations with temperature (Fig. 8) and salinity (Figs. 4 and 8). The cause of this
552 apparent discrepancy is due to the formation of aqueous chloride and hydroxyl complexes, and
553 therefore the association of the Nd^{3+} aqua ion with Cl^- and OH^- ligands (Eqs. 9-16). The
554 stabilization of the Nd chloride and hydroxyl species reduces the calculated activities of Nd^{3+} and
555 hence drive the $NdPO_4$ dissolution reaction in Eq. 4 to the right. Further investigations of the
556 thermodynamic constants for REE chloride and hydroxyl species are therefore essential to
557 accurately predict the solubility of monazite in supercritical fluids. Nevertheless, the new logK_{sp}
558 functions derived in this study (Table 6) provide a means to predict the solubility behavior of
559 $NdPO_4$ at elevated temperature.

560

561 4.4. *Geological significance in peralkaline granitic systems: controls of pH, salinity, and*
562 *temperature on monazite solubility*

563 Acidic saline hydrothermal fluids exsolving from crystallizing magma bodies have the
564 potential to mobilize REE and other incompatible elements. Plutonic rock types associated with
565 magmatic-hydrothermal REE deposits include A-type peralkaline granitic intrusions (e.g.,
566 Khaldzan-Buregtey, Mongolia, Kovalenko et al., 1995; Bokan Mountain, Alaska, USA, Dostal et
567 al., 2014) and biotite-bearing granite and pegmatites (e.g., Capitan Pluton, New Mexico, USA;
568 Banks et al., 1994). Here, the Strange Lake REE-Zr-Nb deposit is used as a case study to emphasize
569 the importance of experimentally determined monazite solubility data in supercritical NaCl-

570 bearing fluids for interpreting controls on REE mobility and ore formation in hydrothermal-
571 magmatic systems.

572 The Strange Lake peralkaline granitic system is host to a world-class REE-Zr-Nb deposit
573 with a strong hydrothermal overprint that led to REE mobilization and further enrichment in
574 hydrothermal alteration zones around pegmatites (Gysi et al., 2013, 2016; Vasyukova and
575 Williams-Jones, 2018). The primary mineralogy consists of feldspar, arfvedsonite, quartz,
576 zironosilicates and secondary Zr- and REE-minerals including zircon, gittinsite, allanite,
577 gadolinite, fluorocarbonates and REE-enriched fluorite (e.g., Gysi et al., 2013, 2016). Although
578 Strange Lake is not a phosphorous-rich system, monazite is observed in this deposit, and also
579 commonly found in other (per)alkaline granitic to syenitic REE deposits, such as Nechalacho in
580 Canada (Sheard et al., 2012; Möller and Williams-Jones, 2016).

581 Numerical simulations were conducted using GEMS to evaluate the controls of pH,
582 temperature, and salinity on monazite solubility at conditions relevant to peralkaline granitic
583 systems using Strange Lake as a case study (Fig. 9). In the simulations, a saline hydrothermal
584 acidic fluid with 0.1-1 mNaCl, 0.01 mHCl and 0.01 mP was equilibrated with a Strange Lake
585 average pegmatite bulk composition taken from the study by Gysi et al. (2013). The major
586 components of the pegmatite include Na-K-Ca-Fe-Al-Si-REE-Zr-F-O-H, which were used to
587 buffer the fluid using a fluid to rock ratio of 1. The mobility of REE is assumed to be controlled
588 by the solubility of REE phosphate solid solutions (monazite and xenotime) and REE fluorides.
589 This rock buffered system was used to model the equilibrium alteration mineralogy of the
590 pegmatite, the pH of the fluid, and the solubility of monazite (using $NdPO_4$ as a proxy for REE
591 mobility) and two different salinities (0.1 and 1 mNaCl). In one fluid, 1 mHCl was added to
592 investigate monazite solubility for an acidic fluid buffered system.

593 The simulated alteration mineralogy (Fig. 9A) reproduces closely field observations (Gysi
594 et al., 2013, 2016) with the presence of quartz, alkali feldspar, plagioclase, hematite and aegirine
595 in the rock buffered altered pegmatite zones, and minerals like zircon, REE fluorides and fluorite
596 typically observed in alteration zones and veins. At rock buffered conditions, the pH in 0.1 and 1
597 mNaCl fluids ranges between ~4.9−5.5 at 450 °C and increases to ~7−7.5 at 700 °C. The higher
598 salinity fluids typically result in slightly lower calculated pH values (Fig. 9B). In contrast, addition
599 of 1 mHCl reduces the pH to ~4.25 at 450 °C and to ~5 at 700 °C for a fluid buffered model, due
600 to an excess amount of protons (H^+) released from the acids. The fluid buffered model overcomes
601 neutralization by cations released from the rock (e.g. K^+, Ca^{2+}, etc.), even at a fluid to rock ratio
602 of 1.

603 Salinity and pH of the fluid have a strong effect on the simulated monazite solubility (Fig.
604 9C). In the rock buffered model with 0.01 mHCl and 0.1 m NaCl, the logarithm $mNdPO_4$ increases
605 between 450 to 700 °C but remains below log $mNdPO_4$ values of -7.5. Increasing NaCl
606 concentrations of the fluid to 1 mNaCl results in an increase of $NdPO_4$ solubility by ~1 to 2.5
607 orders of magnitude due to formation of Nd chloride aqueous species despite the rock buffered pH
608 of these two fluids. In contrast, addition of 1 mNaCl and 1 mHCl (i.e., fluid buffed low pH values)
609 results in another increase of solubility above log $mNdPO_4$ values of ~ -5 to -4.5 indicating that
610 the REE are more mobile in acidic saline fluids, which is in line with the modeling study by Gysi
611 et al. (2013). However, the simulations considerably underestimate the solubility of monazite (Fig.
612 9C) because the thermodynamic properties of REE chloride aqueous species at such high
613 temperature and pressure conditions require revision. This becomes apparent when comparing the
614 simulated $NdPO_4$ solubility with the calculated values using the empirical fits from Eqs. 7-8. The
615 calculated log $mNdPO_4$ values are ~4 to 6 orders of magnitude higher than the simulated monazite

616 solubility at equivalent salinity of 0.1 mNaCl. Furthermore, the empirical fits display a much
617 steeper solubility increase with temperature in the comparison to the simulations that level off at
618 temperatures > 550−600 °C. Further addition of NaCl and using empirical fits from Eqs. 7-8 would
619 result in a solubility reversal (not shown in this figure), where $NdPO_4$ solubility becomes
620 retrograde and decreases with temperature. This behavior is not captured in the simulations, partly
621 because the simulations are buffered by rock forming minerals which affects the pH and because
622 they are more complex with several REE phosphate and fluoride phases controlling REE solubility.
623 Therefore, this shift from REE chloride (more soluble) to REE hydroxyl (less soluble) controlled
624 aqueous speciation and the solubility reversal are not captured by current thermodynamic models.
625 These processes could prove to be important for the mobilization/precipitation mechanisms of
626 REE in natural geologic systems in highly saline fluids at temperatures >500 °C.
627
628 **5. CONCLUSION**

629 We measured $NdPO_4$ solubility at 500, 600 and 700 °C and 1.7 kbar pressure using gold
630 capsules in cold-seal pressure vessels combined with the isotope dilution technique. Measured
631 $NdPO_4$ solubility ranges from 28.2 ppm to 10858 ppm and varies as a function of temperature and
632 salinity. At 500 °C, there is a linear correlation between $NdPO_4$ molality and mCl with a slope of
633 1.2, indicating that the $NdCl^{2+}$ is predominant and controls $NdPO_4$ solubility. The slope derived
634 from the linear correlation of $mNdPO_4$ and mCl gradually decreases to 0.5 and 0 at 600 and 700
635 °C, respectively indicating that $NdCl^{2+}$ becomes less stable at these experimental conditions and
636 $Nd(OH)_3^0$ becomes predominant.

637 The average stoichiometry determined from linear correlation of log $mNdPO_4$ with log
638 mCl and pH are supported by speciation calculations using GEMS. In the experiments with
639 pH<6.7, increasing salinity promotes $NdPO_4$ dissolution, due to increasing chloride ion activity
640 and the stabilization of aqueous $NdCl^{+2}$. In experiments with pH>6.7, chloride complexes
641 destabilize, owing to its increased association with H^+ and Na^+, which produces in the solubility
642 trend reversal and the dominance of hydroxyl complexes. We used speciation calculations to re-
643 evaluate and optimize values of solubility equilibrium constants ($\log K_{sp}$) for $NdPO_4$ using our
644 experiments and experimental results compiled from the literature. These updated log K_{sp} values
645 can be used to improve modeling predictions for the solubility of $NdPO_4$ in supercritical fluids.

646 We conducted a series of numerical simulations of fluid-rock interaction between saline
647 fluids and a Strange Lake felsic intrusion to assess the differences between predicted and
648 empirically determined $NdPO_4$ solubility at high temperature. The simulations underestimate
649 $NdPO_4$ solubility by 4-6 orders of magnitude at high temperature, indicating that the
650 thermodynamic data for Nd chloride species requires revision. The results demonstrate that Cl-
651 bearing exsolved fluids from crystallizing plutons have the potential to mobilize large amounts of
652 light REE at high temperature and may play an important role in redistributing REE in areas
653 adjacent to cooling plutons.

654

655 **ACKNOWLEDGMENTS**

656 This research is based upon work supported by the U.S. Department of Energy, Office of
657 Science, Office of Basic Energy Sciences, Geosciences program under Award Number DE-

SC0022269 to LW, APG, NH, AM and CZ. We would like to extend our sincerest gratitude towards Dr. H. Han and B. Frey at the Analytical Chemistry Laboratory, New Mexico Bureau of Geology and Mineral Resources, for assistance with ICP-OES and ICP-MS instruments. Dr. Nels Iverson is thanked for his assistance with FE-SEM. Dr. F. Ramos is thanked for his guidance and assistance for conducting MC-ICP-MS at the Johnson Mass Spectrometer Lab, New Mexico State University, Las Cruces, NM. We would like to thank our reviewers, D. Foustoukos and two anonymous reviewers, the associate editor, Kono Lemke, for their constructive feedback on the paper. We also express our gratitude towards the executive editor, Jeffrey Catalano for handling our manuscript.

CRediT STATEMENT

Debarati Banerjee: Conceptualization, Methodology, Validation, Formal Analysis, Investigation, Writing-Original Draft, Writing-Review and Editing, Visualization. **Laura E. Waters**: Conceptualization, Methodology, Validation, Formal Analysis, Investigation, Resources, Data Curation, Writing-Original Draft, Writing-Review and Editing, Visualization, Supervision, Funding Acquisition. **Nicole C. Hurtig**: Conceptualization, Methodology, Formal Analysis, Resources, Writing-Review and Editing, Funding Acquisition. **Alexander P. Gysi**: Conceptualization, Methodology, Software, Validation, Formal Analysis, Resources, Data Curation, Writing-Review and Editing, Visualization, Project Administration, Funding Acquisition. **Daniel Harlov**: Methodology, Resources, Writing-Review and Editing. **Chen Zhu**: Conceptualization, Methodology, Writing-Review and Editing, Funding Acquisition. **Artaches Migdisov**: Conceptualization, Writing-Review and Editing, Funding Acquisition.

APPENDIX A. SUPPLEMENTARY MATERIAL

Supplementary Materials include two tables and one figure. The tables include regular spike measurements through time via ICP-MS to monitor the stability of the spike (Table S1) and the masses involved in creation of the experimental solutions (Table S2) from section 2.1. We also include a supplementary figure (Figure S1) that addresses the workflow for sample extraction following the experiment.

DATA AVAIVABILITY

Data are available through Mendeley Data at https://doi.org/10.17632/ps6xk7mgpr.1.

References

Audétat, A., Pettke, T., Heinrich, C. A., & Bodnar, R. J. (2008). Special Paper: The Composition of Magmatic-Hydrothermal Fluids in Barren and Mineralized Intrusions. *Economic Geology*, *103*, 877–908.

Audétat, A. (2019). The Metal Content of Magmatic-Hydrothermal Fluids and Its Relationship to Mineralization Potential. *Economic Geology*, *114*, 1033–1056.

Ayers, J. C., & Watson, E. B. (1991). Solubility of apatite, monazite, zircon, and rutile in supercritical aqueous fluids with implications for subduction zone geochemistry. *Philosophical Transactions of the Royal Society of London. Series A: Physical and Engineering Sciences*, *335*, 365–375.

Balaram, V. (2019). Rare earth elements: A review of applications, occurrence, exploration, analysis, recycling, and environmental impact. *Geoscience Frontiers*, *10*, 1285–1303.

Banks, D. A., Yardley, B. W. D., Campbell, A. R., & Jarvis, K. E. (1994). REE composition of an aqueous magmatic fluid: A fluid inclusion study from the Capitan Pluton, New Mexico, U.S.A. *Chemical Geology*, *113*, 259–272.

Candela, P. A., & Piccoli, P. M. (1998). Magmatic Contributions to Hydrothermal Ore Deposits: An Algorithm (MVPart) for Calculating the Composition of the Magmatic Volatile Phase. In J. P. Richards & P. B. Larson (Eds.), *Techniques in Hydrothermal Ore Deposits Geology* (Vol. 10, p. 0). Society of Economic Geologists.

Cetiner, Z. S., Wood, S. A., & Gammons, C. H. (2005). The aqueous geochemistry of the rare earth elements. Part XIV. The solubility of rare earth element phosphates from 23 to 150 °C. *Chemical Geology*, *217*, 147–169.

Chakhmouradian, A. R., & Wall, F. (2012). Rare Earth Elements: Minerals, Mines, Magnets (and More). *Elements*, *8*, 333–340.

Cherniak, D. J., Pyle, J., & Rakovan, J. (2004). Synthesis of REE and Y phosphates by Pb-free flux methods and their utilization as standards for electron microprobe analysis and in design of monazite chemical U-Th-Pb dating protocol. *American Mineralogist*, *89*, 1533–1539.

Dhote, P., Bhan, U., & Verma, D. (2021). Genetic model of carbonatite hosted rare earth elements mineralization from Ambadongar Carbonatite Complex, Deccan Volcanic Province, India. *Ore Geology Reviews*, *135*, 104215.

Diakonov, I. I., Ragnarsdottir, K. V., & Tagirov, B. R. (1998). Standard thermodynamic properties and heat capacity equations of rare earth hydroxides: II. Ce(III)-, Pr-, Sm-, Eu(III)-, Gd-,

725 Tb-, Dy-, Ho-, Er-, Tm-, Yb-, and Y-hydroxides. Comparison of thermochemical and
726 solubility data. *Chemical Geology*, *151*, 327–347.
727 Dostal, J., Kontak, D. J., & Karl, S. M. (2014). The Early Jurassic Bokan Mountain peralkaline
728 granitic complex (southeastern Alaska): Geochemistry, petrogenesis and rare-metal
729 mineralization. *Lithos*, *202–203*, 395–412.
730 Driesner, T., & Heinrich, C. A. (2007). The system H2O–NaCl. Part I: Correlation formulae for
731 phase relations in temperature–pressure–composition space from 0 to 1000°C, 0 to
732 5000bar, and 0 to 1 X_{NaCl}. *Geochimica et Cosmochimica Acta*, *71*, 4880–4901.
733 Fan, H.-R., Yang, K.-F., Hu, F.-F., Liu, S., & Wang, K.-Y. (2016). The giant Bayan Obo REE-
734 Nb-Fe deposit, China: Controversy and ore genesis. *Geoscience Frontiers*, *7*, 335–344.
735 Gammons, C. H., Wood, S.A., Youning, L. (2002). Complexation of the rare earth elements with
736 aqueous chloride at 200° and 300°C and saturated water vapor pressure. *Water-Rock*
737 *Interaction, Ore Deposits, Environmental Geochemistry*, 191-207.
738 Gibert, F., & Montel, J. M. (1996). Etude expérimentale de la solubilité de la monazite dans les
739 fluides à H_2O-CO_2. *Réunion des Sciences de la Terre*.
740 Goodenough, K. M., Wall, F., & Merriman, D. (2018). The Rare Earth Elements: Demand, Global
741 Resources, and Challenges for Resourcing Future Generations. *Natural Resources*
742 *Research*, *27*, 201–216.
743 Guan, Q., Mei, Y., Etschmann, B., Testemale, D., Louvel, M., & Brugger, J. (2020). Yttrium
744 complexation and hydration in chloride-rich hydrothermal fluids: A combined ab initio
745 molecular dynamics and in situ X-ray absorption spectroscopy study. *Geochimica et*
746 *Cosmochimica Acta*, *281*, 168–189.

747 Guan, Q., Mei, Y., Etschmann, B., Louvel, M., Testemale, D., Bastrakov, E., & Brugger, J. (2022).
748 Yttrium speciation in sulfate-rich hydrothermal ore-forming fluids. *Geochimica et*
749 *Cosmochimica Acta*, *325*, 278–295.
750 Gysi, A. P., & Williams-Jones, A. E. (2013). Hydrothermal mobilization of pegmatite-hosted REE
751 and Zr at Strange Lake, Canada: A reaction path model. Geochimica et Cosmochimica
752 Acta, 122, 324-352.
753 Gysi, A. P., Williams-Jones, A. E., & Harlov, D. (2015). The solubility of xenotime-(Y) and other
754 HREE phosphates ($DyPO_4$, $ErPO_4$ and $YbPO_4$) in aqueous solutions from 100 to 250 °C
755 and p sat. *Chemical Geology*, *401*, 83–95.
756 Gysi, A. P., Williams-Jones, A. E., & Collins, P. (2016). Lithogeochemical Vectors for
757 Hydrothermal Processes in the Strange Lake Peralkaline Granitic REE-Zr-Nb Deposit.
758 *Economic Geology*, *111*, 1241–1276.
759 Gysi, A. P., Harlov, D., & Miron, G. D. (2018). The solubility of monazite ($CePO_4$), $SmPO_4$, and
760 $GdPO_4$ in aqueous solutions from 100 to 250 °C. *Geochimica et Cosmochimica Acta*, *242*,
761 143–164.
762 Gysi, A. P., & Harlov, D. (2021). Hydrothermal solubility of $TbPO_4$, $HoPO_4$, $TmPO_4$, and $LuPO_4$
763 xenotime endmembers at pH of 2 and temperatures between 100 and 250 °C. *Chemical*
764 *Geology*, *567*, 120072.
765 Gysi, A. P., Hurtig, N. C., Pan, R., Miron, D. G., & Kulik, D. A. (2023). *MINES thermodynamic*
766 *database, New Mexico Bureau of Geology and Mineral Resources, version 23*.
767 https://geoinfo.nmt.edu/mines-tdb/
768 Haas, J. R., Shock, E. L., & Sassani, D. C. (1995). Rare earth elements in hydrothermal systems:
769 Estimates of standard partial molal thermodynamic properties of aqueous complexes of the

770 rare earth elements at high pressures and temperatures. *Geochimica et Cosmochimica Acta*,
771 *59*, 4329–4350.
772 Harlov, D. E., Meighan, C. J., Kerr, I. D., & Samson, I. M. (2016). Mineralogy, Chemistry, and
773 Fluid-Aided Evolution of the Pea Ridge Fe Oxide-(Y + REE) Deposit, Southeast Missouri,
774 USA*. *Economic Geology*, *111*, 1963–1984.
775 Helgeson, H. C., & Kirkham, D. H. (1974). Theoretical prediction of the thermodynamic behavior
776 of aqueous electrolytes at high pressures and temperatures; II, Debye-Huckel parameters
777 for activity coefficients and relative partial molal properties. *American Journal of Science*,
778 *274*, 1199–1261.
779 Helgeson, H. C., Kirkham, D. H., & Flowers, G. C. (1981). Theoretical prediction of the
780 thermodynamic behavior of aqueous electrolytes by high pressures and temperatures; IV,
781 Calculation of activity coefficients, osmotic coefficients, and apparent molal and standard
782 and relative partial molal properties to 600 degrees C and 5kb. *American Journal of*
783 *Science*, *281*, 1249.
784 Holtstam, D., Andersson, U. B., Broman, C., & Mansfeld, J. (2014). Origin of REE mineralization
785 in the Bastnäs-type Fe-REE-(Cu-Mo-Bi-Au) deposits, Bergslagen, Sweden. *Mineralium*
786 *Deposita*, *49*, 933–966.
787 Johnson, J. W., Oelkers, E. H., & Helgeson, H. C. (1992). SUPCRT92: A software package for
788 calculating the standard molal thermodynamic properties of minerals, gases, aqueous
789 species, and reactions from 1 to 5000 bar and 0 to 1000°C.
790 Kestin, J., Sengers, J. V., Kamgar-Parsi, B., & Sengers, J. M. H. L. (1984). Thermophysical
791 Properties of Fluid H2O. *Journal of Physical and Chemical Reference Data*, *13*, 175–183.

792 Konings, R., Beneš, O., Kovacs, A., Manara, D., Sedmidubský, D., Gorokhov, L., Iorish, V.,
793 Yungman, V., Shenyavskaya, E., & Osina, E. (2014). The Thermodynamic Properties of
794 the f-Elements and their Compounds. Part 2. The Lanthanide and Actinide Oxides. *Journal*
795 *of Physical and Chemical Reference Data*, *43*.
796 Kovalenko, V. I., Tsaryeva, G. M., Goreglyad, A. V., Yarmolyuk, V. V., Troitsky, V. A., Hervig,
797 R. L., & Farmer, G. L. (1995). The peralkaline granite-related Khaldzan-Buregtey rare
798 metal (Zr, Nb, REE) deposit, western Mongolia. *Economic Geology*, *90*, 530–547.
799 Kulik, D. A. (2006). Dual-thermodynamic estimation of stoichiometry and stability of solid
800 solution end members in aqueous–solid solution systems. *Chemical Geology*, *225*, 189–
801 212.
802 Kulik, D. A., Wagner, T., Dmytrieva, S. V., Kosakowski, G., Hingerl, F. F., Chudnenko, K. V., &
803 Berner, U. R. (2013). GEM-Selektor geochemical modeling package: Revised algorithm
804 and GEMS3K numerical kernel for coupled simulation codes. *Computational Geosciences*,
805 *17*, 1–24.
806 Liu, W., Etschmann, B., Migdisov, A., Boukhalfa, H., Testemale, D., Müller, H., Hazemann, J.-
807 L., & Brugger, J. (2017). Revisiting the hydrothermal geochemistry of europium(II/III) in
808 light of new in-situ XAS spectroscopy results. *Chemical Geology*, *459*, 61–74.
809 Liu, Y., Chakhmouradian, A. R., Hou, Z., Song, W., & Kynický, J. (2019). Development of REE
810 mineralization in the giant Maoniuping deposit (Sichuan, China): Insights from
811 mineralogy, fluid inclusions, and trace-element geochemistry. *Mineralium Deposita*, *54*,
812 701–718.

Louvel, M., Bordage, A., Testemale, D., Zhou, L., & Mavrogenes, J. (2015). Hydrothermal controls on the genesis of REE deposits: Insights from an in situ XAS study of Yb solubility and speciation in high temperature fluids (T < 400 °C). *Chemical Geology, 417*, 228–237.

Mayanovic, R. A., Jayanetti, S., Anderson, A. J., Bassett, W. A., & Chou, I.-M. (2002). The Structure of Yb^{3+} Aquo Ion and Chloro Complexes in Aqueous Solutions at Up to 500 °C and 270 MPa. *The Journal of Physical Chemistry A*, *10*, 6591–6599.

Mayanovic, R. A., Anderson, A. J., Bassett, W. A., & Chou, I.-M. (2007). On the formation and structure of rare-earth element complexes in aqueous solutions under hydrothermal conditions with new data on gadolinium aqua and chloro complexes. *Chemical Geology*, *239*, 266–283.

Mayanovic, R., Anderson, A., Bassett, W., & Chou, I.-M. (2008). REE-chloride complexing in hydrothermal fluids with new data on Lanthanum chloroaqua complexes. *Geochimica et Cosmochimica Acta Supplement*, *72*.

Mayanovic, R. A., Anderson, A. J., Bassett, W. A., & Chou, I.-M. (2009). The structure and stability of aqueous rare-earth elements in hydrothermal fluids: New results on neodymium(III) aqua and chloroaqua complexes in aqueous solutions to 500 °C and 520 MPa. *Chemical Geology, 259*, 30–38.

Migdisov, A. A., & Williams-Jones, A. E. (2002). A spectrophotometric study of neodymium(III) complexation in chloride solutions. *Geochimica et Cosmochimica Acta*, *66*, 4311–4323.

Migdisov, Art. A., Williams-Jones, A. E., & Wagner, T. (2009). An experimental study of the solubility and speciation of the Rare Earth Elements (III) in fluoride- and chloride-bearing aqueous solutions at temperatures up to 300°C. *Geochimica et Cosmochimica Acta*, *73*, 7087–7109.

836 Migdisov, A., Williams-Jones, A. E., Brugger, J., & Caporuscio, F. A. (2016). Hydrothermal
837 transport, deposition, and fractionation of the REE: Experimental data and thermodynamic
838 calculations. *Chemical Geology*, *439*, 13–42.
839 Miron, G. D., Kulik, D. A., Dmytrieva, S. V., & Wagner, T. (2015). GEMSFITS: Code package
840 for optimization of geochemical model parameters and inverse modeling. *Applied*
841 *Geochemistry*, *55*, 28–45.
842 Miron, G. D., Wagner, T., Kulik, D. A., & Heinrich, C. A. (2016). Internally consistent
843 thermodynamic data for aqueous species in the system Na–K–Al–Si–O–H–Cl. *Geochimica*
844 *et Cosmochimica Acta*, *187*, 41–78.
845 Möller V. and Williams-Jones A. E. (2016) Petrogenesis of the Nechalacho Layered Suite, Canada:
846 Magmatic Evolution of a REE–Nb-rich Nepheline Syenite Intrusion. *J. Petrology* 57, 229–
847 276.
848 Navrotsky, A., Lee, W., Mielewczyk-Gryn, A., Ushakov, S. V., Anderko, A., Wu, H., & Riman,
849 R. E. (2015). Thermodynamics of solid phases containing rare earth oxides. *The Journal*
850 *of Chemical Thermodynamics*, *88*, 126–141.
851 Oelkers, E. H., & Helgeson, H. C. (1990). Triple-ion anions and polynuclear complexing in
852 supercritical electrolyte solutions. *Geochimica et Cosmochimica Acta*, *54*, 727–738.
853 Pan, R., Gysi, A. P., Miron, G. D., & Zhu, C. (2024). Optimized thermodynamic properties of REE
854 aqueous species (REE^{3+} and $REEOH^{2+}$) and experimental database for modeling the
855 solubility of REE phosphate minerals (monazite, xenotime, and rhabdophane) from 25 to
856 300 °C. Chemical Geology, 643, 121817.
857 Perry, E. P., & Gysi, A. P. (2018). Rare Earth Elements in Mineral Deposits: Speciation in
858 Hydrothermal Fluids and Partitioning in Calcite. *Geofluids*, *2018*, e5382480.

859 Poitrasson, F., Oelkers, E., Schott, J., & Montel, J.-M. (2004). Experimental determination of
860 synthetic $NdPO_4$ monazite end-member solubility in water from 21°C to 300°C:
861 Implications for rare earth element mobility in crustal fluids. *Geochimica et Cosmochimica*
862 *Acta*, *68*, 2207–2221.
863 Popa, K., & Konings, R. J. M. (2006). High-temperature heat capacities of EuPO4 and SmPO4
864 synthetic monazites. *Thermochimica Acta*, *445*, 49–52.
865 Pourtier, E., Devidal, J.-L., & Gibert, F. (2010). Solubility measurements of synthetic neodymium
866 monazite as a function of temperature at 2kbars, and aqueous neodymium speciation in
867 equilibrium with monazite. *Geochimica et Cosmochimica Acta*, *74*, 1872–1891.
868 Robie, R. A., & Hemingway, B. S. (1995). *Thermodynamic Properties of Minerals and Related*
869 *Substances at 298.15 K and 1 Bar (105 Pascals) Pressure and at Higher Temperatures*.
870 U.S. Government Printing Office.
871 Robinson, R. A., & Stokes, R. H. (2002). *Electrolyte solutions*. Courier Corporation.
872 Schmidt, C., Rickers, K., Bilderback, D. H., & Huang, R. (2007). In situ synchrotron-radiation
873 XRF study of REE phosphate dissolution in aqueous fluids to 800 °C. *Lithos*, *95*, 87–102.
874 Sheard E. R., Williams-Jones A. E., Heiligmann M., Pederson C. and Trueman D. L. (2012)
875 Controls on the Concentration of Zirconium, Niobium, and the Rare Earth Elements in the
876 Thor Lake Rare Metal Deposit, Northwest Territories, Canada. *Economic Geology* 107,
877 81–104.
878 Shock, E. L., & Helgeson, H. C. (1988). Calculation of the thermodynamic and transport properties
879 of aqueous species at high pressures and temperatures: Correlation algorithms for ionic
880 species and equation of state predictions to 5 kb and 1000°C. *Geochimica et Cosmochimica*
881 *Acta*, *52*, 2009–2036.

882 Shock, E. L., Helgeson, H. C., & Sverjensky, D. A. (1989). Calculation of the thermodynamic and
883 transport properties of aqueous species at high pressures and temperatures: Standard partial
884 molal properties of inorganic neutral species. *Geochimica et Cosmochimica Acta*, *53*,
885 2157–2183.
886 Shock, E. L., Oelkers, E. H., Johnson, J. W., Sverjensky, D. A., & Helgeson, H. C. (1992).
887 Calculation of the thermodynamic properties of aqueous species at high pressures and
888 temperatures. Effective electrostatic radii, dissociation constants and standard partial molal
889 properties to 1000 °C and 5 kbar. *Journal of the Chemical Society, Faraday Transactions*,
890 *88*, 803–826.
891 Shock, E. L., Sassani, D. C., Willis, M., & Sverjensky, D. A. (1997). Inorganic species in geologic
892 fluids: Correlations among standard molal thermodynamic properties of aqueous ions and
893 hydroxide complexes. *Geochimica et Cosmochimica Acta*, *61*, 907–950.
894 Shu, X., & Liu, Y. (2019). Fluid inclusion constraints on the hydrothermal evolution of the
895 Dalucao Carbonatite-related REE deposit, Sichuan Province, China. *Ore Geology Reviews*,
896 *107*, 41–57.
897 Singh, Y., Mundra, K., Jagadeesan, P., Rai, S. D., & Verma, M. (2018). Characteristics of Source
898 Rocks of Xenotime-Bearing Riverine Placers in Central India. *Exploration and Research*
899 *for Atomic Minerals*, *27*, 145–162.
900 Tagirov, B. R., Zotov, A. V., & Akinfiev, N. N. (1997). Experimental study of dissociation of HCl
901 from 350 to 500°C and from 500 to 2500 bars: Thermodynamic properties of HCl°(aq).
902 *Geochimica et Cosmochimica Acta*, *61*, 4267–4280.
903 Tanaka, T., Togashi, S., Kamioka, H., Amakawa, H., Kagami, H., Hamamoto, T., Yuhara, M.,
904 Orihashi, Y., Yoneda, S., Shimizu, H., Kunimaru, T., Takahashi, K., Yanagi, T., Nakano,

905 T., Fujimaki, H., Shinjo, R., Asahara, Y., Tanimizu, M., & Dragusanu, C. (2000). JNdi-1:
906 A neodymium isotopic reference in consistency with LaJolla neodymium. *Chemical*
907 *Geology*, *168*, 279–281.
908 Tanger, J. C., & Helgeson, H. C. (1988). Calculation of the thermodynamic and transport
909 properties of aqueous species at high pressures and temperatures; revised equations of state
910 for the standard partial molal properties of ions and electrolytes. *American Journal of*
911 *Science*, *288*, 19–98.
912 Tanis, E.A., Simon, A., Tschauner, O., Chow, P., Xiao, Y., Shen, G., Hanchar, J.M., Frank, M.,
913 2012. Solubility of xenotime in a 2 M HCl aqueous fluid from 1.2 to 2.6 GPa and 300 to
914 500 °C. American Mineralogist 97, 1708–1713.
915 Thiriet, C., Konings, R. J. M., Javorský, P., Magnani, N., & F. Wastin. (2005). The low
916 temperature heat capacity of LaPO4 and GdPO4, the thermodynamic functions of the
917 monazite-type $LnPO_4$ series. *The Journal of Chemical Thermodynamics*, *37*, 131–139.
918 Tillberg, M., Maskenskaya, O. M., Drake, H., Hogmalm, J. K., Broman, C., Fallick, A. E., &
919 Åström, M. E. (2019). Fractionation of Rare Earth Elements in Greisen and Hydrothermal
920 Veins Related to A-Type Magmatism. *Geofluids*, *2019*, e4523214.
921 Ushakov, S. V., Helean, K. B., Navrotsky, A., & Boatner, L. A. (2001). Thermochemistry of rare-
922 earth orthophosphates. *Journal of Materials Research*, *16*, 2623–2633.
923 Van Hoozen, C. J., Gysi, A. P., & Harlov, D. E. (2020). The solubility of monazite ($LaPO_4$, $PrPO_4$,
924 $NdPO_4$, and $EuPO_4$) endmembers in aqueous solutions from 100 to 250 °C. *Geochimica et*
925 *Cosmochimica Acta*, *280*, 302–316.

926 Vasyukova, O. V., Williams-Jones, A. E., & Blamey, N. J. F. (2016). Fluid evolution in the Strange
927 Lake granitic pluton, Canada: Implications for HFSE mobilisation. *Chemical Geology*,
928 *444*, 83–100.
929 Vasyukova, O. V., & Williams-Jones, A. E. (2018). Direct measurement of metal concentrations
930 in fluid inclusions, a tale of hydrothermal alteration and REE ore formation from Strange
931 Lake, Canada. *Chemical Geology*, *483*, 385–396.
932 Venezky, D. Y., & Rutherford, M. J. (1999). Petrology and Fe–Ti oxide reequilibration of the 1991
933 Mount Unzen mixed magma. *Journal of Volcanology and Geothermal Research*, *89*, 213–
934 230.
935 Verplanck, P. L., Lang Farmer, G., Kettler, R. M., Lowers, H. A., Johnson, C. A., Koenig, A. E.,
936 and Blessington, M. J. (2022). Petrogenesis and rare earth element mineralization of the
937 Elk Creek carbonatite, Nebraska, USA. *Ore Geology Reviews*, *146*, 104953.
938 Wagner, T., Kulik, D. A., Hingerl, F. F., & Dmytrieva, S. V. (2012). GEM-SELEKTOR
939 geochemical modeling package: TSolMod library and data interface for multicomponent
940 phase models. *The Canadian Mineralogist*, *50*, 1173–1195.
941 Waters, L. E., Andrews, B. J., & Lange, R. A. (2015). Rapid Crystallization of Plagioclase
942 Phenocrysts in Silicic Melts during Fluid-saturated Ascent: Phase Equilibrium and
943 Decompression Experiments. *Journal of Petrology*, *56*, 981–1006.
944 Williams-Jones, A. E., Samson, I. M., & Olivo, G. R. (2000). The Genesis of Hydrothermal
945 Fluorite-REE Deposits in the Gallinas Mountains, New Mexico. *Economic Geology*, *95*,
946 327–341.
947 Zhilong, H., Cheng, X., McCAIG, A., Congqiang, L., Jing, W., Deru, X., Wenbo, L., Tao, G., &
948 Huayun, X. (2007). REE Geochemistry of Fluorite from the Maoniuping REE Deposit,

949 Sichuan Province, China: Implications for the Source of Ore-forming Fluids. *Acta*
950 *Geologica Sinica - English Edition*, *81*, 622–636.
951 Zhukova, I. A., Stepanov, A. S., Jiang, S.-Y., Murphy, D., Mavrogenes, J., Allen, C., Chen, W., &
952 Bottrill, R. (2021). Complex REE systematics of carbonatites and weathering products
953 from uniquely rich Mount Weld REE deposit, Western Australia. *Ore Geology Reviews*,
954 *139*, 104539.

955 **Figure Captions:**

956 Figure 1: Photomicrographs and SEM images of unreacted (A – B) and reacted (C – D) synthetic
957 $NdPO_4$ crystals at 500, 600, and 700 °C. (A – B) Unreacted crystals are monoclinic and exhibit
958 clean sharp edges. (C – D) The reacted crystals have turned brittle and show the development of
959 dissolution textures with the formation of etched surfaces and rounded edges. (E – F) Secondary
960 $NdPO_4$ precipitates upon quenching on the capsule walls.

961

962 Figure 2: Schematic illustration of the Nd isotope dilution technique used to measure dissolved
963 $NdPO_4$ concentrations in the experiments. The capsule contains initially a solution with known
964 quantity of Nd spiked experimental solution ($^{145}Nd/^{144}Nd = 87.065 \pm 0.005$), whereas the $NdPO_4$
965 has a lower natural isotopic $^{145}Nd/^{144}Nd$ ratio of 0.348412 ± 0.000004. As the $NdPO_4$ dissolves at
966 the experimental temperature and pressure, the natural $^{145}Nd/^{144}Nd$ ratio from $NdPO_4$ dilutes the
967 enriched spike $^{145}Nd/^{144}Nd$. Upon quenching of the experiments, the resulting $^{145}Nd/^{144}Nd$ ratio in
968 the reacted experimental solution will have the same ratio as secondary $NdPO_4$.

969

970 Figure 3: $NdPO_4$ solubility (log $mNdPO_4$; Table 2) as a function of (A) temperature (°C) and (B)
971 salinity (mNaCl). Colors represent different experimental temperatures and symbols represent
972 different NaCl concentrations. The solubility increases from 500 to 700 °C and with increased
973 salinity to 0.05 mNaCl. In (A), the lines joining the experiments with the same salinities are strictly
974 for better visualization of the data. In (B), solubility data are fitted as a function of salinity using

975 Eq. 6, where m and c are defined as functions of temperature represented in (C), using Eq. 7 and
976 8.

977

978 Figure 4: Logarithmic molality of $NdPO_4$ plotted against logarithmic chlorinity and pH at (A, B)
979 500 °C, (C, D) 600 °C and (E) 700 °C. Slopes from linear regressions indicate the average
980 stoichiometry of Nd speciation reactions with chlorine and hydroxyl groups (Eq. 9-16). $NdPO_4$
981 solubility increases with salinity at 500 and 600 °C. At 700 °C, calculated pH becomes unreliable
982 due to uncertainties in thermodynamic properties of polyphosphate species and aqueous Nd
983 species (F).

984

985 Figure 5: Logarithmic function of activities of the aqueous Nd^{+3} (A), $NdCl^{2+}$ (B),
986 $NdCl_2^{+}$ (C), $Nd(OH)^{2+}$ (D) $Nd(OH)_2^{+}$ (E), $Nd(OH)_3^{0}$ (F) species as function of experimental pH,
987 at 500 and 600°C and 1.7 kbar. Calculations were carried out using the GEMS code package and
988 the MINES thermodynamic database with results listed in Table 3. The color and symbol code
989 are the same as in Figure 3.

990

991 Figure 6: Calculated equilibrium pH (A) and REE solid saturation indices (SI) for $Nd(OH)_3$ (B),
992 $NdPO_4$ (C) and Nd_2O_3 (D), as a function of NaCl concentrations (mol/kg) and temperature between
993 500 and 700 °C at 1.7 kbar. Values plotting above the line indicate supersaturation and values
994 below the line under saturation with the respective REE solids. Calculations were carried out using

995 the GEMS code package and the MINES thermodynamic database with results listed in Table 4.
996 The color and symbol code are the same as in Figure 3.

997

998 Figure 7: Logarithm of the molality of dissolved $NdPO_4$ (log $mNdPO_4$) versus temperature (°C)
999 between 500 and 700 °C at 1.7 kbar derived in this study in comparison to predicted curves
1000 calculated using GEMS and existing thermodynamic properties for REE extrapolated from low
1001 temperature data. Details about other experimental studies are summarized in Table 5 and include
1002 solubility measurements by Van Hoozen et al. (2020) in perchloric acid based aqueous solutions
1003 between 100 and 250 °C at saturated water vapor pressure; Poitrasson et al. (2004) in hydrochloric
1004 acid based aqueous solutions between 200 and 300 °C at saturated water vapor pressure; Pourtier
1005 et al. (2004) in pure H_2O and NaCl-HCl-H_2O solutions at 2 kbar and between 300 and 800 °C.

1006

1007 Figure 8: Logarithm of the solubility product (Qsp) of $NdPO_4$ as a function of 1000/T (where T is
1008 in Kelvin) derived from the solubility data in this study and a compilation of experimental studies
1009 summarized in Table 5. The solubility product corresponds to Eq. 6. Fitted functions for the
1010 empirical logK_{sp}-T relationships are summarized in Table 6.

1011

1012 Figure 9: The equilibrium alteration mineralogy (A) predicted to occur between a peralkaline
1013 granitic system (pegmatite) and acidic saline fluids in a fluid rock ratio of 1 is shown as a function
1014 of temperature. The pH range of the a 0.1 mNaCl/0.01 mHCl system (blue), a 1 mNaCl/0.01 mHCl
1015 system (red), and a 1 mNaCl/1 mHCl system (green) (B) are shown as temperature increases from

450 to 700 °C. Predicted monazite solubility for each system in (B) are shown with the calculated monazite solubility (black) using the empirical fits from Eqs. 7-8 (C).

Table 1: Natural abundance of the Nd isotopes and isotopic composition of the ^{145}Nd enriched spike.

Isotope	Natural abundance (%)	Abundance in spike (%)[1]
^{142}Nd	27.15 ± 4	0.3163 ± 0.0007
^{143}Nd	12.17 ± 2.6	4.59 ± 0.01
^{144}Nd	23.79 ± 1.9	1.047 ± 0.002
^{145}Nd	8.29 ± 1.2	91.2 ± 0.2
^{146}Nd	17.19 ± 3.2	2.676 ± 0.006
^{148}Nd	5.76 ± 2.1	0.1265 ± 0.0002
^{150}Nd	5.64 ± 2.8	0.063 ± 0.002

[1] The isotope abundance in the spike is measured via MC-ICP-MS

Table 2: Measured $^{145}Nd/^{144}Nd$ ratio via MC-ICP-MS and total dissolved $NdPO_4$ at 500-700°C and 1.7 kbar and errors.

Runs	T	Time	Crystal	Solution	Nd spike[1]	error[2]	mNaCl[3]	mHCl	$^{145}Nd/^{144}Nd$	error[4]	dissolved $NdPO_4$	error[5]	experimental error[6]	log ($mNdPO_4$)[7]
	(°C)	(hours)	(mg)	(mg)	(ppm)	%	(mol/kg)	(mol/kg)		%	(ppm)	%	%	(mol/kg)
EF4-9	500	168	22.4	90.56	0.253	2	N/A	0.01	0.375410	0.22	59	2	6	-3.61
EF4-11	500	96	18.4	72.89	0.253	2	N/A	0.01	0.404918	0.05	28.2	2	6	-3.93
EF4-13	500	96	13.48	94.95	0.253	2	N/A	0.01	0.369697	0.04	74.9	2	6	-3.50
EF4-12	600	96	16.5	65.56	0.253	2	N/A	0.01	0.351303	0.01	557	2	6	-2.63
EF4-5	700	168	11.2	38.97	0.253	2	N/A	0.01	0.349295	0.01	1875	2	6	-2.11
EF2-2	500	168	7.9	77.51	0.263	0.7	0.05	0.01	0.351274	0.01	585	0.7	6	-2.61
EF2-4	600	96	7.6	65.87	0.263	0.7	0.05	0.01	0.350029	0.03	1045	0.7	6	-2.36
EF2-5	700	96	17.9	45.61	0.263	0.7	0.05	0.01	0.348598	0.002	10858	0.7	6	-1.34
EF1-7	500	96	10.2	83.03	0.251	0.7	0.5	0.01	0.348709	0.003	6000	0.7	6	-1.60
EF1-3	600	168	8.7	58.87	0.251	0.7	0.5	0.01	0.348944	0.01	3169	0.7	6	-1.88
EF1-4	700	168	14.3	58.21	0.251	0.7	0.5	0.01	0.349965	0.03	1040	0.7	6	-2.36

[1] Nd spike concentration is measured via ICP-MS and the corresponding error percentage on the final spike concentration.
[2] The RSD value calculated from repeated analysis of the spike
[3] The final NaCl concentration is measured by the ICP-OES.
[4] The error in percentage on the measured $^{145}Nd/^{144}Nd$ occurring as a result of mass bias on the MC-ICP-MS
[5] The final propagated error (percentage) on the final total dissolved $NdPO_4$ is also given
[6] The RSD value calculated on the measured log $mNdPO_4$
[7] The $^{145}Nd/^{144}Nd$ isotope ratio is obtained using MC-ICP-MS, which is then use to solved for the moles of dissolved Nd in the experimental solutions contributed by the $NdPO_4$ only at experimental conditions. Since the molar ratio of Nd to $NdPO_4$ is 1:1, the total moles of dissolved Nd is the direct measure of the total dissolved $NdPO_4$, which we report as the logarithm of moles of $NdPO_4$ dissolved (log $mNdPO_4$).

1037
1038

1039

Table 3: Calculated pH and aqueous Nd and P species activities (*a*) at 500-700°C and 1.7 kbar.

Runs	T (°C)	$pH_{T,P}$[1]	I[2]	log $a Nd^{+3}$	log $a NdCl^{+2}$	log $a NdCl_2^{+}$	log $a NdOH^{+2}$	log $a Nd(OH)_2^{+}$	log $a Nd(OH)_3^{0}$	log $a NaOH$	log $a NaCl$	log $a HCl$	log $a Cl^{-}$	log $a HPO_4^{-2}$	log $a H_2PO_4^{-}$	log $a H_3PO_4^{0}$	log $a PO_4^{-3}$	log $a H_2P_2O_7^{-2}$	log $a HP_2O_7^{-3}$
									0 mNaCl										
EF4-9	500	2.5	0.004	-9.40	-3.96	-7.71	-7.74	-8.62	-11.32	N/A	N/A	-2.25	-2.47	-12.89	-5.95	-3.62	-24.47	-8.59	-15.02
EF4-11	500	2.5	0.004	-9.70	-4.27	-8.03	-8.07	-8.97	-11.69	N/A	N/A	-2.23	-2.48	-13.25	-6.29	-3.93	-24.86	-9.27	-15.72
EF4-13	500	2.5	0.004	-9.30	-3.86	-7.61	-7.63	-8.50	-11.18	N/A	N/A	-2.26	-2.47	-12.76	-5.83	-3.51	-24.33	-8.36	-14.77
EF4-12	600	4.2	0.007	-11.17	-3.24	-7.69	-7.32	-6.40	-7.70	N/A	N/A	-2.50	-2.50	-10.64	-4.41	-2.81	-21.52	-4.74	-10.42
EF4-5	700	6.7	0.12	-13.73	-3.50	-8.88	-7.10	-3.65	-2.78	N/A	N/A	-3.73	-2.70	-8.90	-4.22	-4.14	-18.17	-3.68	-7.78
									0.05 mNaCl										
EF2-2	500	3.7	0.04	-9.89	-3.59	-6.47	-7.08	-6.81	-8.36	-6.59	-1.91	-2.53	-1.61	-9.78	-3.98	-2.80	-20.21	-4.66	-9.94
EF2-4	600	5.4	0.04	-12.22	-3.62	-7.39	-7.20	-5.10	-5.22	-4.90	-1.62	-3.00	-1.82	-9.08	-4.02	-3.61	-18.77	-3.98	-8.48
EF2-5	700	7.4	0.13	-14.68	-4.12	-9.15	-7.37	-3.22	-1.67	-3.04	-1.67	-4.08	-2.36	-8.48	-4.49	-5.10	-17.05	-4.21	-7.62
									0.5 mNaCl										
EF1-7	500	6.1	0.34	-10.71	-3.82	-6.12	-5.52	-2.87	-2.03	-3.57	-0.69	-4.33	-1.02	-7.00	-3.60	-4.80	-15.05	-3.89	-6.78
EF1-3	600	6.7	0.22	-13.41	-4.29	-7.54	-7.06	-3.63	-2.42	-2.99	-0.52	-3.81	-1.31	-8.03	-4.30	-5.22	-16.39	-4.53	-7.70
EF1-4	700	6.7	0.1	-15.90	-4.60	-8.90	-9.26	-5.78	-4.89	-3.17	-0.40	-2.68	-1.63	-9.51	-4.85	-4.79	-18.75	-4.93	-9.01

[1] Calculations were carried out at each conditions using the GEMS code package and the MINES thermodynamic database.

[2] The Ionic Strength (I) calculated at the experimental conditions using the GEMS code package and the MINES thermodynamic database.

1040
1041
1042
1043

Table 4: Calculated reaction quotient (log Q_{sp}) for the solubility of $NdPO_4$ and saturation indices of REE solids (*SI*) at 500-700°C and 1.7 kbar.

Runs	T (°C)	log Q_{sp}[1]	*SI* ($NdPO_4$)	*SI* (Nd_2O_3)	*SI* ($Nd(OH)_3$)
			no NaCl		
EF4-9	500	-33.87	4.02	-14.31	-4.85
EF4-11	500	-34.56	3.34	-15.05	-5.22
EF4-13	500	-33.63	4.27	-14.04	-4.71
EF4-12	600	-32.68	8.81	-3.73	-0.34
EF4-5	700	-31.89	12.96	9.26	5.51
			0.05 m NaCl		
EF2-2	500	-30.10	7.80	-8.40	-1.89
EF2-4	600	-31.00	10.49	1.23	2.14
EF2-5	700	-31.73	13.12	11.50	6.63
			0.5 m NaCl		
EF1-7	500	-25.76	12.13	4.27	4.43
EF1-3	600	-29.80	11.69	6.83	4.93
EF1-4	700	-34.65	10.21	5.05	3.40

[1] Calculations were carried out at each temperature and 1.7 kbar using the GEMS code package and the MINES thermodynamic database.

Table 5: $NdPO_4$ solubility studies between 100 and 800 °C and saturated water vapor pressure to 2 kbar.

Study	$NdPO_4$ physical state	Experimental apparatus	Solution chemistry	pH	T (°C)	P (kbar)	Reported dominant Nd-aqueous species
Gilbert and Montel (1996)	crystal	EHPV- weight loss method[1]	H_2O	4.5	540-800	2	$Nd(OH)_2^{+}$*
Poitrasson et al. (2004)	crystal	Batch-type solubility experiments	H_2O-HCl	2	200-300	0	Nd^{+3}, $NdCl^{+2}$
Cetiner et al. (2005)	powder	Batch-type solubility experiments	H_2O+NaCl+HCl H_2O+$NaClO_4$+$HClO_4$	1, 0-2	150	0	Nd^{+3}
Pourtier et al. (2010)	crystal	EHPV-I.D.-T.I.M.S[2]	H_2O,	1-8	300	2	$Nd(OH)^{+2}$
			H_2O-NaCl±HCl±NaOH	4.5	650	2	$Nd(OH)_3^0$
Van Hoozen et al. (2020)	crystal	Batch-type solubility experiments	H_2O+$HClO_4$+H_3PO_4	2	100-250	0	Nd^{+3}, $Nd(OH)^{+2}$
This study	crystal	EHPV-I.D.-M.C.I.C.P.M.S[3]	H_2O+HCl±NaCl	2.5-6.5	500-700	1.7	$NdCl^{+2}$, $Nd(OH)_3^0$

[1]Externally heated pressure vessel experiments coupled with weight loss method.
[2]Externally heated pressure vessel coupled with isotope dilution and Thermal Ionization Mass Spectrometry.
[3]Externally heated (cold seal) pressure vessel coupled with isotope dilution and Multi-Collector Inductively Coupled Plasma Mass Spectrometry
*Calculated in this study

Table 6. Fit coefficients for log $K_{sp}(NdPO_4)$ = A + BT +C/T.

Reference	T (°C)	P (kbar)	A	B	C	R^2
Van Hoozen et al. (2020); Cetiner et al. (2005); Poitrasson et al. (2004)	100−300	P_{sat}	9.833 *(19.52)*[1]	-0.060 *(0.02)*	-5769 *(4386)*	0.85
This study; Pourtier et al. (2010); Gilbert and Montel (1996)	300−700	1.7 – 2.0	41.81 *(38.77)*	-0.057 *(0.026)*	-20987 *(13952)*	0.44

[1]Standard uncertainty for each fit coefficient given in italics beneath each value

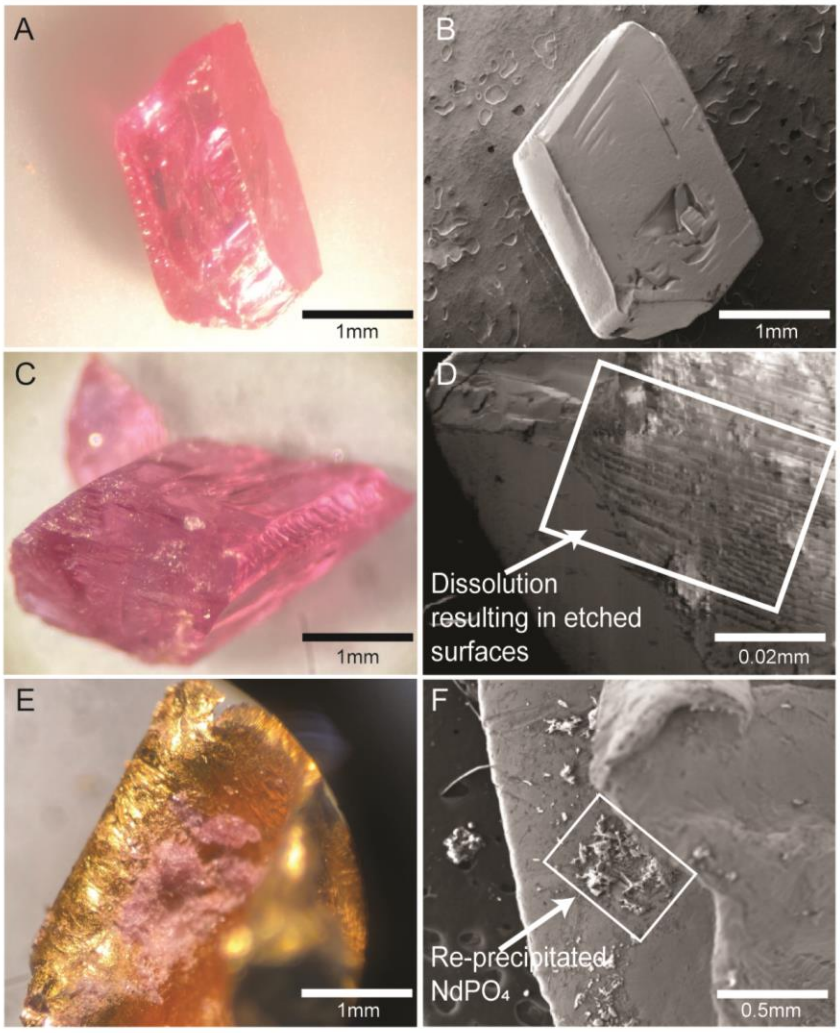
A
1mm
B
1mm
C
1mm
D
Dissolution
resulting in etched
surfaces
0.02mm
E
1mm
F
Re-precipitated
NdPO4
0.5mm

Figure 1:

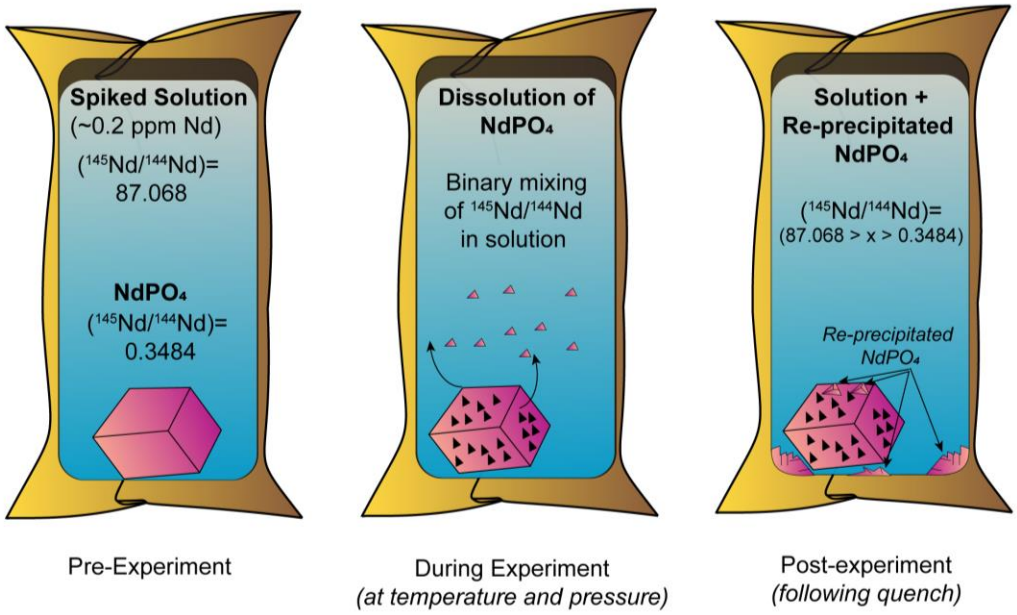
Spiked Solution
(~0.2 ppm Nd)
(145Nd/144Nd)=
87.068
NdPO4
(145Nd/144Nd)=
0.3484
Dissolution of
NdPO4
Binary mixing
of 145Nd/144Nd
in solution
Solution +
Re-precipitated
NdPO4
(145Nd/144Nd)=
(87.068 > x > 0.3484)
Re-precipitated
NdPO4
Pre-Experiment
During Experiment
(at temperature and pressure)
Post-experiment
(following quench)

Figure 2

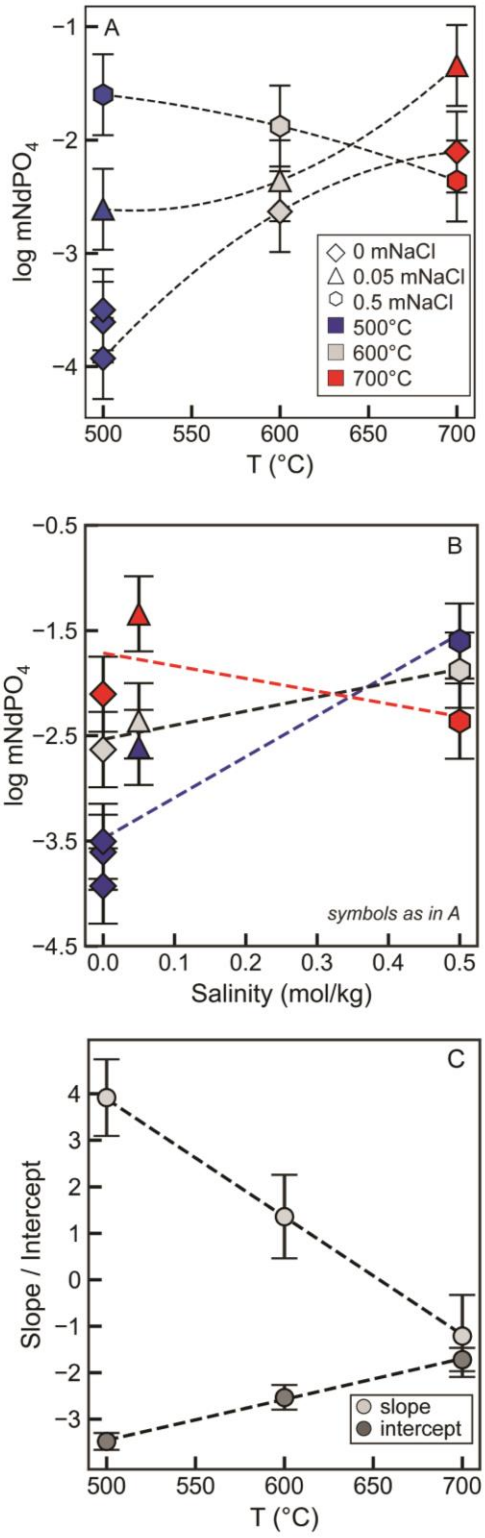
A
log mNdPO4
T (°C)
0 mNaCl
0.05 mNaCl
0.5 mNaCl
500°C
600°C
700°C
B
log mNdPO4
Salinity (mol/kg)
symbols as in A
C
Slope / Intercept
T (°C)
slope
intercept

Figure 3:

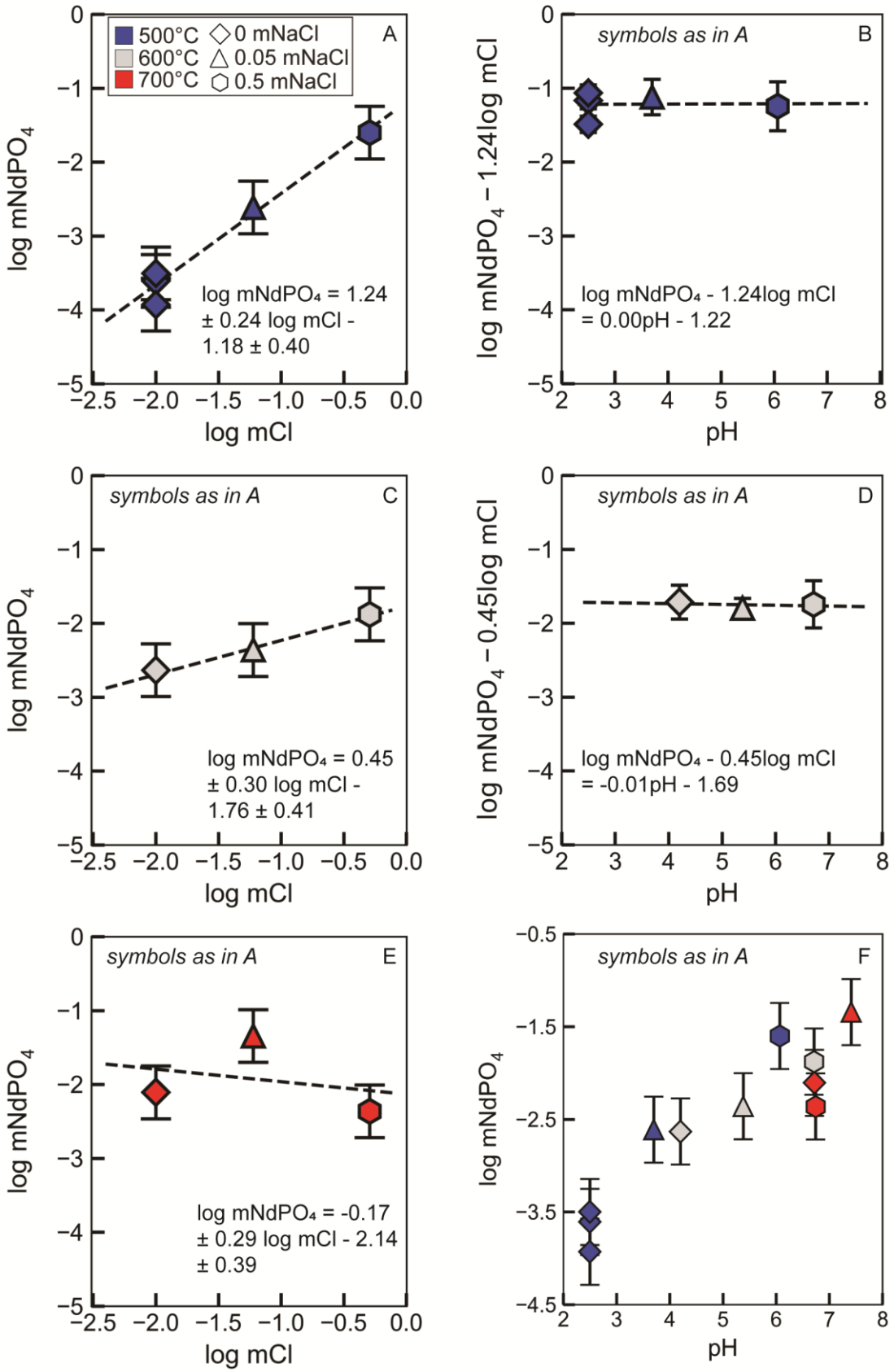
500°C
600°C
700°C
0 mNaCl
0.05 mNaCl
0.5 mNaCl
A
log mNdPO4 = 1.24 ± 0.24 log mCl - 1.18 ± 0.40
log mNdPO4
log mCl
symbols as in A
B
log mNdPO4 - 1.24log mCl = 0.00pH - 1.22
log mNdPO4 – 1.24log mCl
pH
C
log mNdPO4 = 0.45 ± 0.30 log mCl - 1.76 ± 0.41
D
log mNdPO4 - 0.45log mCl = -0.01pH - 1.69
log mNdPO4 – 0.45log mCl
E
log mNdPO4 = -0.17 ± 0.29 log mCl - 2.14 ± 0.39
F

Figure 4:

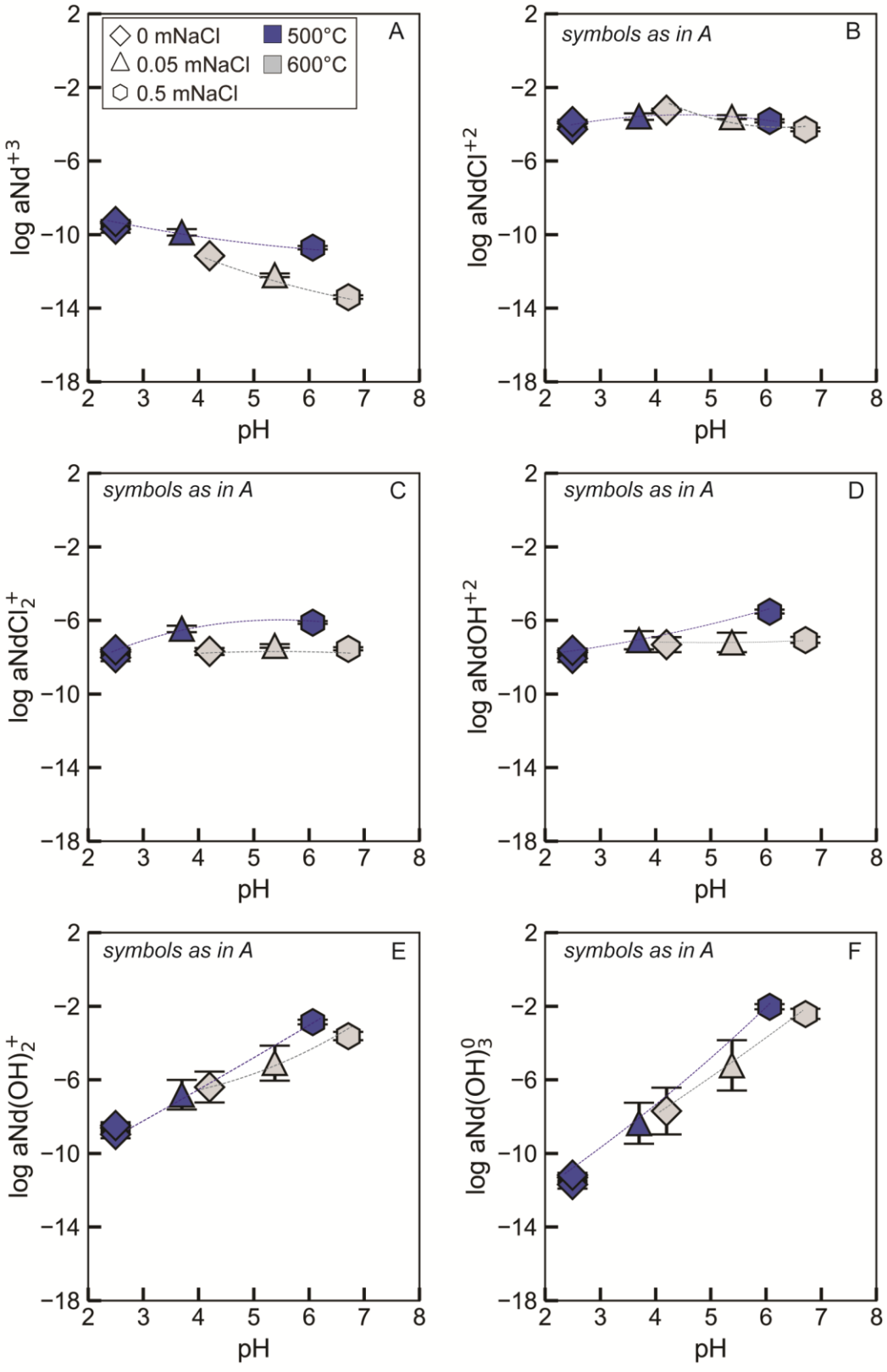
0 mNaCl
0.05 mNaCl
0.5 mNaCl
500°C
600°C
A
B
C
D
E
F
symbols as in A
log aNd+3
log aNdCl+2
log aNdCl2+
log aNdOH+2
log aNd(OH)2+
log aNd(OH)30
pH
2
−2
−6
−10
−14
−18
3
4
5
6
7
8

Figure 5:

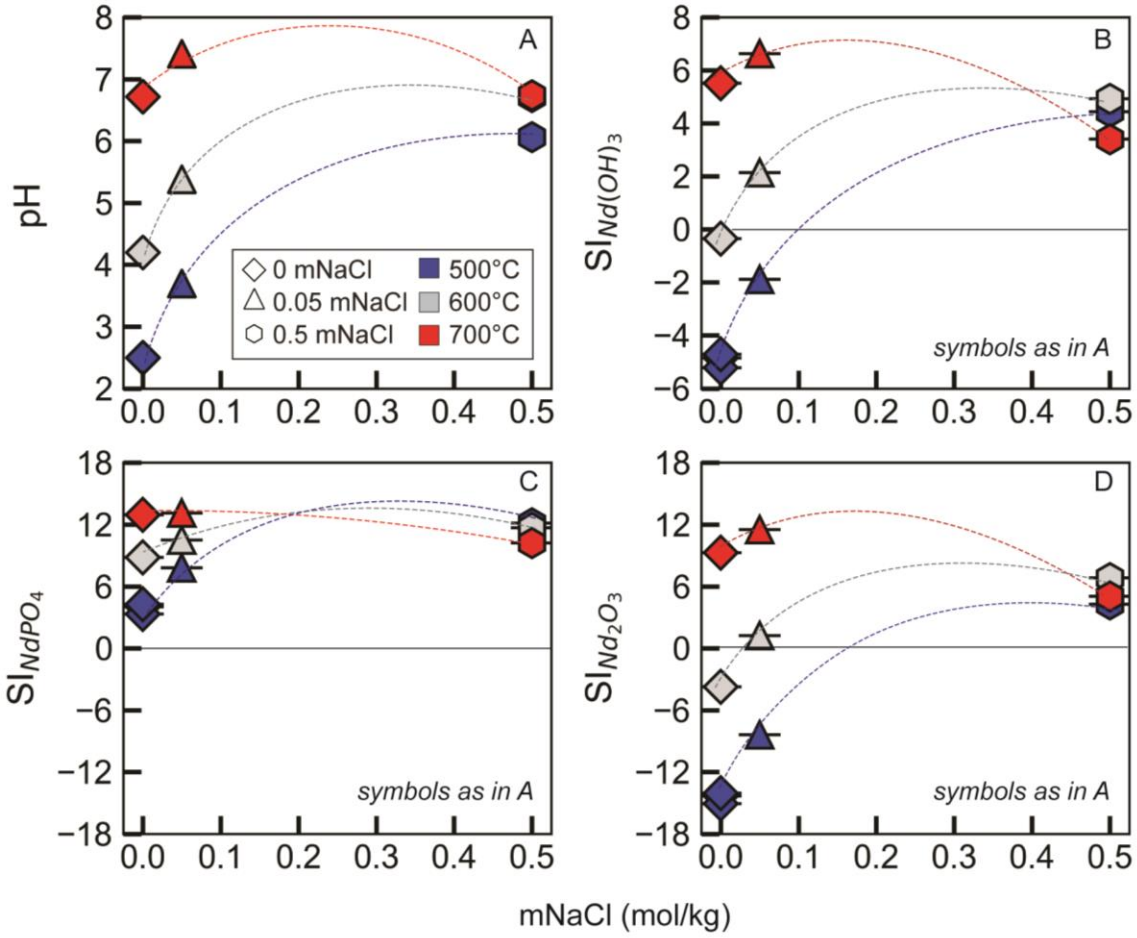
A
B
C
D
pH
SI$_{Nd(OH)_3}$
SI$_{NdPO_4}$
SI$_{Nd_2O_3}$
0 mNaCl
0.05 mNaCl
0.5 mNaCl
500°C
600°C
700°C
symbols as in A
mNaCl (mol/kg)

Figure 6

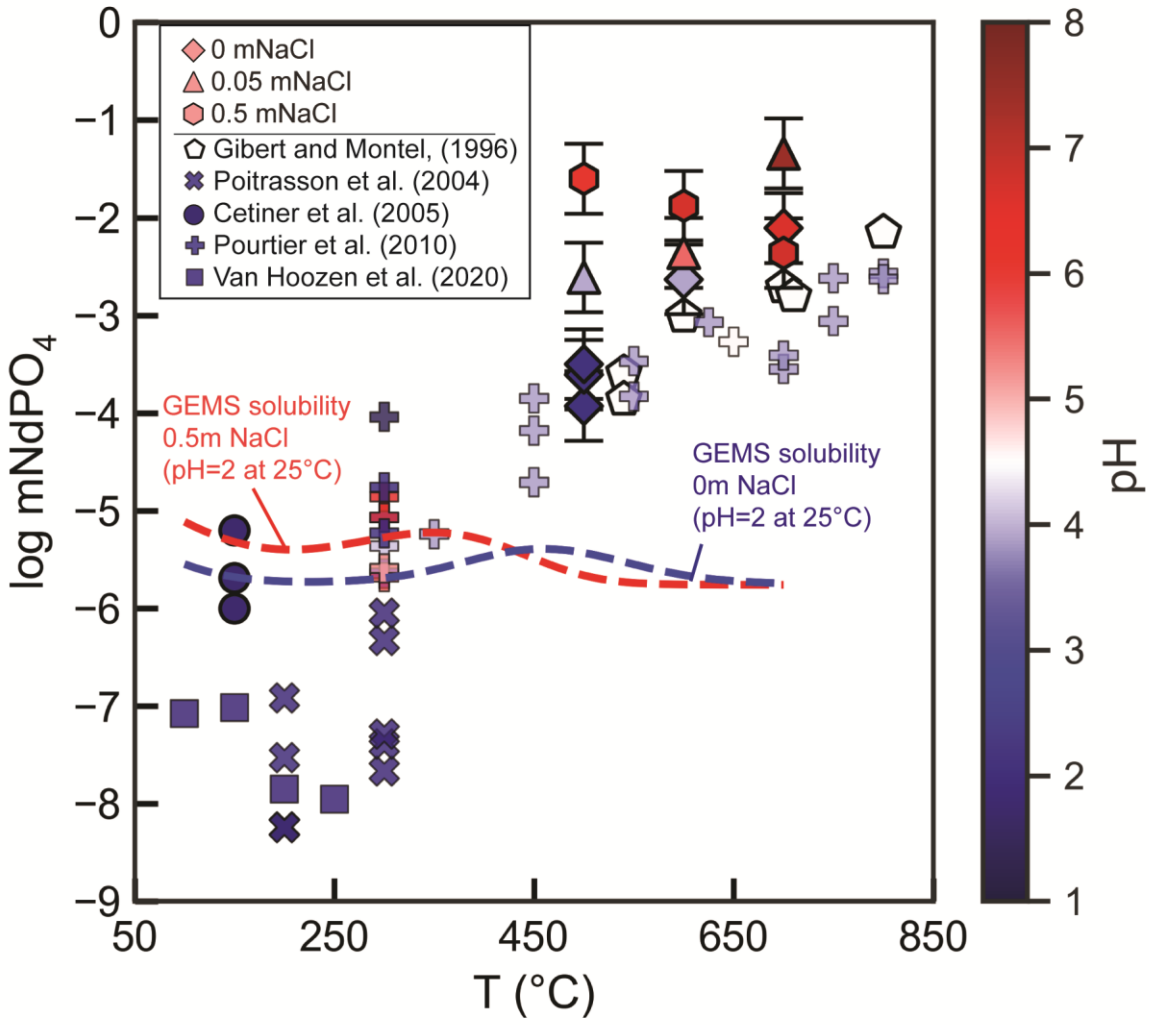
0 mNaCl
0.05 mNaCl
0.5 mNaCl
Gibert and Montel, (1996)
Poitrasson et al. (2004)
Cetiner et al. (2005)
Pourtier et al. (2010)
Van Hoozen et al. (2020)
GEMS solubility
0.5m NaCl
(pH=2 at 25°C)
GEMS solubility
0m NaCl
(pH=2 at 25°C)
log mNdPO4
T (°C)
pH
0
−1
−2
−3
−4
−5
−6
−7
−8
−9
50
250
450
650
850
8
7
6
5
4
3
2
1

Figure 7:

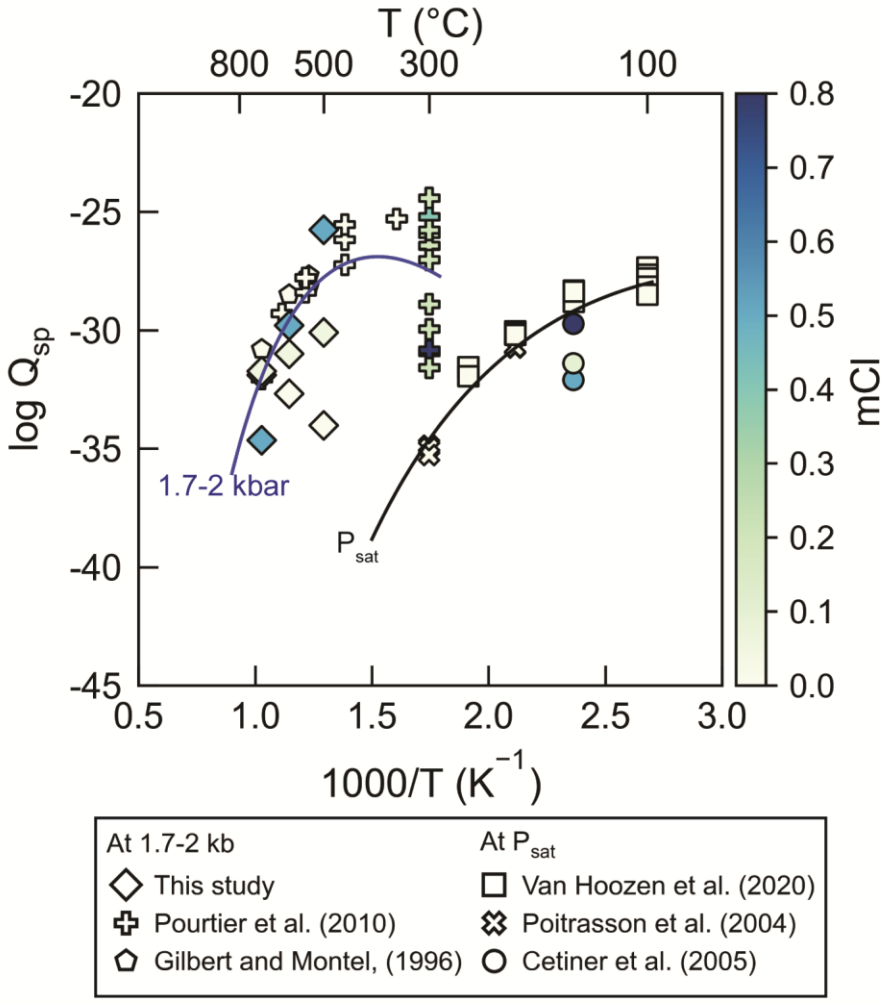
T (°C)
800
500
300
100
-20
-25
-30
-35
-40
-45
log Q_{sp}
0.5
1.0
1.5
2.0
2.5
3.0
1000/T (K^{-1})
0.8
0.7
0.6
0.5
0.4
0.3
0.2
0.1
0.0
mCl
1.7-2 kbar
P_{sat}
At 1.7-2 kb
This study
Pourtier et al. (2010)
Gilbert and Montel, (1996)
At P_{sat}
Van Hoozen et al. (2020)
Poitrasson et al. (2004)
Cetiner et al. (2005)

Figure 8:

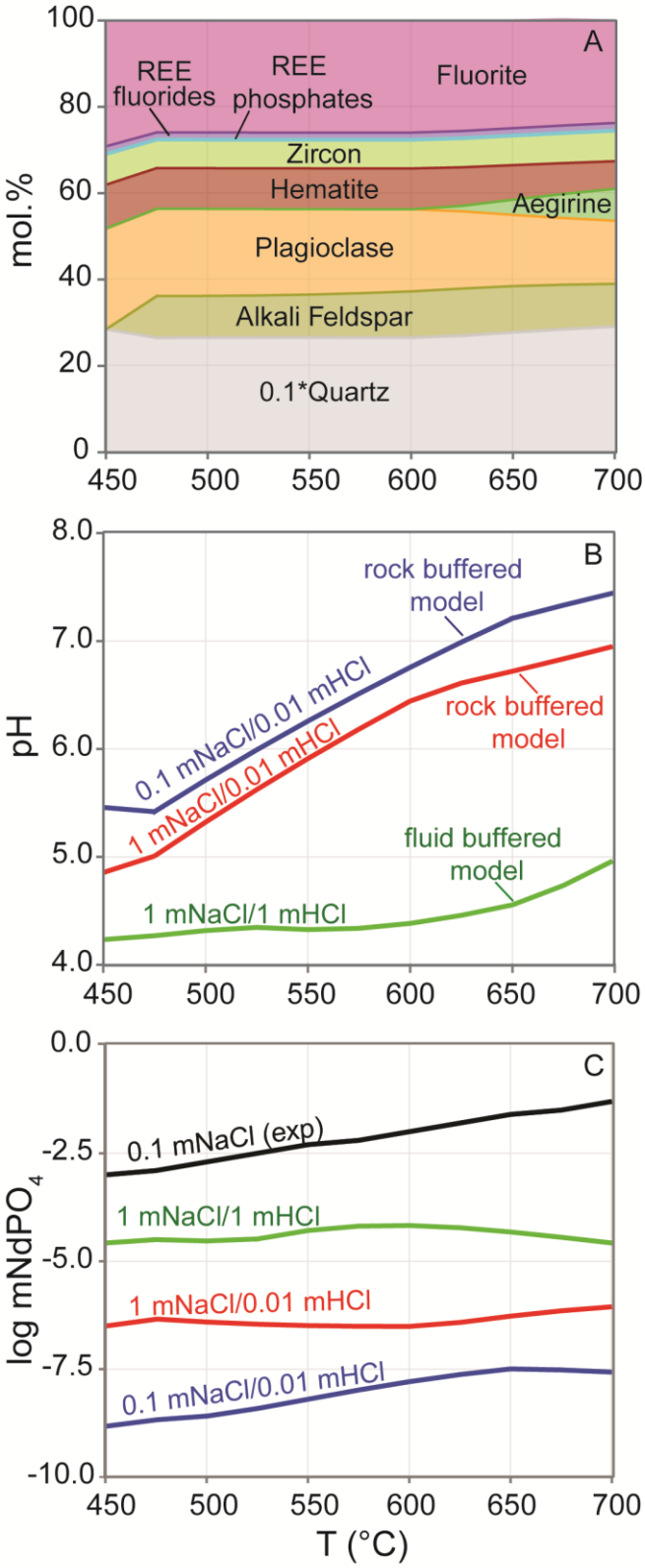
A
REE fluorides
REE phosphates
Fluorite
Zircon
Hematite
Aegirine
Plagioclase
Alkali Feldspar
0.1*Quartz
mol.%
100
80
60
40
20
0
450
500
550
600
650
700
B
rock buffered model
0.1 mNaCl/0.01 mHCl
1 mNaCl/0.01 mHCl
rock buffered model
fluid buffered model
1 mNaCl/1 mHCl
pH
8.0
7.0
6.0
5.0
4.0
C
0.1 mNaCl (exp)
1 mNaCl/1 mHCl
1 mNaCl/0.01 mHCl
0.1 mNaCl/0.01 mHCl
log mNdPO4
0.0
-2.5
-5.0
-7.5
-10.0
T (°C)

Figure 9

Supplementary Material

Table S1: The spike concentration of each of the experimental solutions measured at regular intervals via ICP-MS at ambient conditions (P= 1b and T=25°C)

Experiment(s)	Nd spike (ppm)	Average	standard deviation	RSD %
EF-1	0.253			
	0.252	0.252		
	0.250	0.252		
	0.249	0.251	0.00178	0.708
EF-2	0.264			
	0.264	0.264		
	0.261	0.263	0.00182	0.691
EF-4	0.260			
	0.252	0.256		
	0.249	0.254		
	0.252	0.253	0.00462	1.824

Table S2: Preparation of the initial NaCl solution which has then been used to prepare the experimental solutions for carrying out the solubility experiments between 500 and 700°C and 1.7 kbar pressure.

Name	NaCl (g/mol)	NaCl (g)	milliQ (g)	Add Stock-1 (g)	Add Stock-2 (g)	0.1 mHCl (g)	Total mass (g)	NaCl (mol/kg)	HCl (mol/kg)	Spike (ppm)	Final NaCl (mol/kg)	Final HCl (mol/ kg)
Stock-1	58.44	5.004	100.3				100.3	0.85				
Stock-2			89.99	10.05			100.04	0.09				
EF-1				90.06		10.01	100.07	0.77	0.01	0.251	0.5	0.01
EF-2					89.95	9.99	99.94	0.08	0.01	0.263	0.05	0.01
EF-4			90.13			10.01	100.14		0.01	0.253	0	0.01

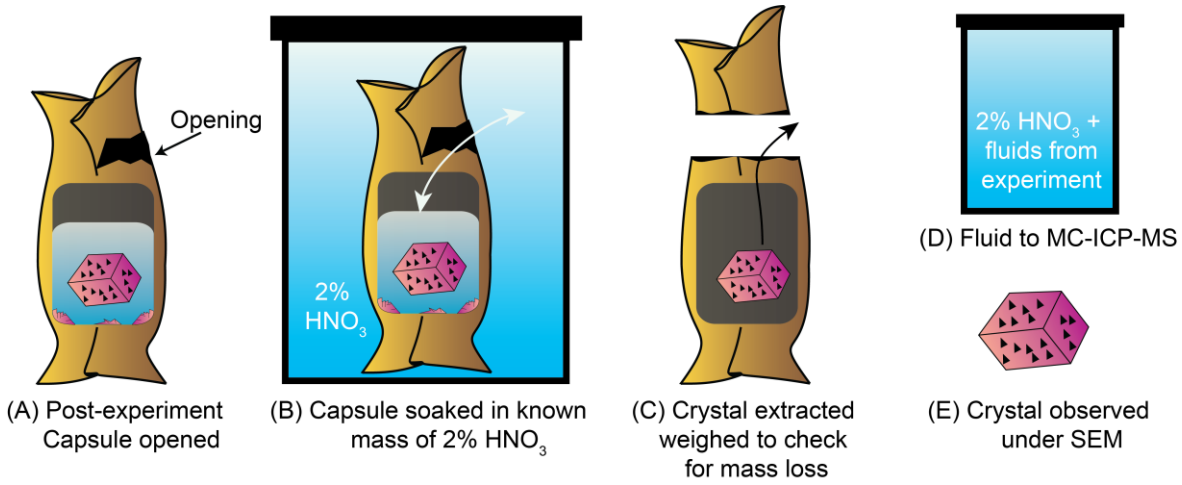

Figure S3: Post Experiment Crystal and Fluid Extraction. As can be seen from left to right, the capsule is first opened at one of its neck (A) and sonicated in 2% nitric acid (B), following which the capsule is peeled open to extract the crystal (C). Post extraction, the fluid is analyzed by MC-ICP-MS (D) and the crystal is imaged SEM (E).

Table S4: The standard Gibbs energy of formation (ΔfG^0) for the aqueous species calculated at the experimental conditions using the MINES thermodynamic database and GEMS code package.

Species	ΔfG^0 (J/mol) at 1.7 kbar and			References
	500 °C	600 °C	700 °C	
$NdPO_4$(s)	-1933917	-1959634	-1987055	Ushakov et al. (2001), Thiriet et al. (2005), Popa and Konings, (2006), Ni et al. (1995)
Nd^{+3}	-804062	-819619	-842073	Pan et al., (2024)
$PO4^{-3}$	-812706	-736998	-652066	Supcrt92, slop98.dat
H2O	-285075	-299358	-314533	Johnson et al. (1992)
H^+	0	0	0	Supcrt92, slop98.dat
OH^-	-130021	-116702	-100324	Supcrt92, slop98.dat
Cl^-	-126698	-116215	-101883	Supcrt92, slop98.dat
$NdCl^{+2}$	-804062	-819619	-842073	Migdisov et al. (2009)
$NdCl_2^+$	-911910	-903252	-894142	Migdisov et al. (2009)
$NdOH^{+2}$	-833151	-823277	-813171	Supcrt92, slop98.dat
$Nd(OH)_2^+$	-782694	-768504	-752387	Supcrt92, slop98.dat
$Nd(OH)_3$	-991109	-976686	-958907	Supcrt92, slop98.dat
HPO_4^{-2}	-1021598	-989013	-949812	Supcrt92, slop98.dat
$H_2PO_4^-$	-1161843	-1163497	-1162182	Supcrt92, slop98.dat
$H_3PO_4^0$	-1233789	-1260383	-1288833	Supcrt92, slop98.dat
Na^+	-297498	-308556	-320234	Miron et al. (2016)
$NaCl^0$	-444283	-459900	-475775	Miron et al. (2016)
HCl^0	-189797	-210973	-232612	Tagirov et al. (1997)
$NaOH^0$	-455807	-468578	-481916	Miron et al. (2016)
$H_4P_2O_7^0$	-2202602	-2253507	-2308923	Supcrt92, slop98.dat
$H_3P_2O_7^-$	-2144841	-2172853	-2199719	Supcrt92, slop98.dat
$H_2P_2O_7^{-2}$	-2086715	-2094811	-2097572	Supcrt92, slop98.dat
$HP_2O_7^{-3}$	-1954117	-1929624	-1896012	Supcrt92, slop98.dat
$P_2O_7^{-4}$	-1737034	-1658897	-1567213	Supcrt92, slop98.dat

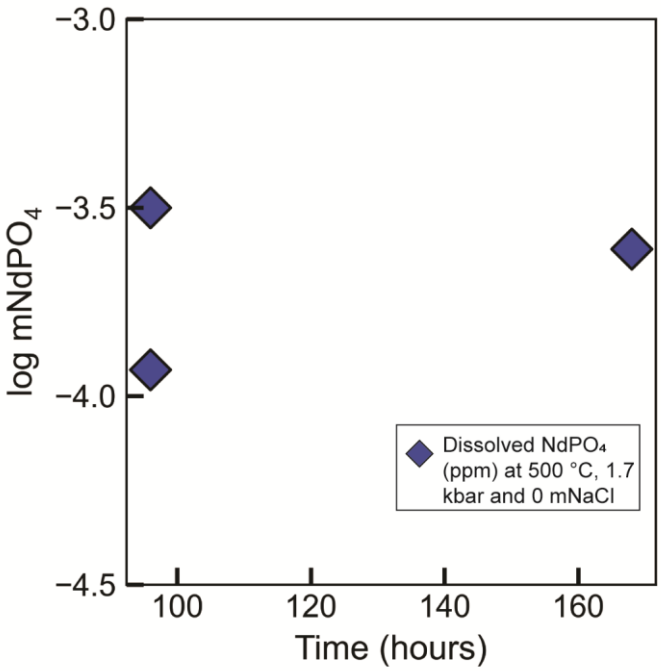

Figure S5: The logarithmic function of total moles of dissolved $NdPO_4$ at 500 °C, 1.7 kbar and mNaCl concentration, versus time (hours).

Table S6: Calculated pH , ionic strength (I) and aqueous Nd and P species activities (*a*) at experimental temperatures and pressures for the experimental studies in use via the GEMS code package and the updated MINES thermodynamic database

Runs	$pH_{T,P}$[1]	$pH_{T,P}$[2]	ΔpH[3]	I	log $a Nd^{+3}$	log $a NdCl^{+2}$	log $a NdCl_2^{+}$	log $a NdOH^{+2}$	log $a Nd(OH)_2^{+}$	log $a Nd(OH)_3^{0}$	log aNaOH	log aNaCl	log aHCl	log aCl	log $a HPO_4^{-2}$	log $a H_2PO_4^{-}$	log $a H_3PO_4^{0}$	log $a PO_4^{-3}$	log $a H_2P_2O_7^{-2}$	log $a HP_2O_7^{-3}$
Cetiner et al. (2005) at 150 °C and a Psat																				
Nd-I1-150	1.3	1.1	0.22	0.88	-7.76	-7.89	-7.09	-11.60	-15.93	-20.76	-10.51	-0.89	-2.13	-0.28	-11.01	-4.79	-3.18	-21.97	-9.93	-15.57
Nd-I05-150	1.3	1.1	0.21	0.46	-7.90	-8.29	-7.75	-11.75	-16.11	-20.96	-10.84	-1.47	-2.37	-0.55	-13.21	-6.97	-5.33	-24.20	-14.29	-19.96
Nd-I01-150	1.2	1.1	0.15	0.10	-7.38	-8.37	-8.44	-11.31	-15.76	-20.68	-12.44	-3.59	-2.89	-1.15	-12.95	-6.62	-4.90	-24.02	-13.60	-19.35
Gibert and Montel, 1996 at 540 °C and 2 kbar																				
FG_2	5.1	4.5	0.62	0.00	-10.27	-10.61	-21.37	-5.83	-4.08	-4.30	N/A	N/A	N/A	N/A	-8.73	-4.23	-4.37	-17.89	-4.86	-8.846
FG_1	5.1	4.5	0.57	0.00	-9.90	-10.27	-21.05	-5.50	-3.80	-4.06	N/A	N/A	N/A	N/A	-8.59	-4.04	-4.13	-17.79	-4.48	-8.512
Gibert and Montel, 1996 at 600 °C and 2 kbar																				
FG_3	5.2	4.5	0.69	0.00	-9.96	-9.39	-21.08	-5.12	-3.22	-3.54	N/A	N/A	N/A	N/A	-8.89	-3.92	-3.63	-18.54	-3.6	-8.521
Gibert and Montel, 1996 at 700 °C and 2 kbar																				
FG_4	5.6	4.5	1.08	0.00	-10.93	-9.39	-23.15	-5.30	-2.96	-3.24	N/A	N/A	N/A	N/A	-9.67	-4.17	-3.41	-19.88	-3.78	-8.208
Poitrasson et al. (2004) at 200 °C and Psat																				
Nd200-pH2_3	2.0	2.0	0.03	0.01	-8.92	-9.76	-10.70	-10.84	-13.73	-17.28	N/A	N/A	-4.18	-2.04	-11.28	-5.45	-4.21	-21.82	-10.6	-15.83
Nd200-pH2_2	2.0	2.0	0.03	0.01	-8.91	-9.75	-10.69	-10.83	-13.72	-17.27	N/A	N/A	-4.18	-2.04	-11.27	-5.44	-4.20	-21.81	-10.6	-15.8
Nd200-pH2_1	2.0	2.0	0.03	0.01	-8.91	-9.75	-10.69	-10.83	-13.72	-17.27	N/A	N/A	-4.18	-2.04	-11.25	-5.43	-4.19	-21.79	-10.5	-15.78
Poitrasson et al. (2004) at 300 °C and Psat																				
Nd300-pH2_3	2.1	2.0	0.12	0.01	-9.57	-7.78	-8.73	-9.67	-11.52	-14.52	N/A	N/A	-2.91	-2.07	-13.71	-6.84	-4.65	-25.30	-12.2	-18.45
Nd300-pH2_2	2.1	2.0	0.12	0.01	-9.67	-7.89	-8.83	-9.78	-11.62	-14.63	N/A	N/A	-2.91	-2.07	-13.71	-6.84	-4.65	-25.30	-12.2	-18.45
Nd300-pH2_1	2.1	2.0	0.12	0.01	-9.95	-8.16	-9.10	-10.05	-11.90	-14.90	N/A	N/A	-2.91	-2.07	-13.74	-6.87	-4.67	-25.33	-12.2	-18.49
Pourtier et al. (2010) at 350 °C and 2 kbar, in H_2O																				
M-98-16	5	4.5	0.5	1E-05	-9.41	-14.19	-23.5	-6.66	-5.55	-5.56	N/A	N/A	-13.36	-9	-8.3	-5.26	-6.66	-15.88	-8.569	-11.22
Pourtier et al. (2010) at 450 °C and 2 kbar, in H_2O																				
M-98-4	4.9	4.5	0.4	6E-05	-9.34	-11.79	-21.87	-5.74	-4.4	-4.63	N/A	N/A	-12.01	-9.01	-8.27	-4.31	-4.91	-16.83	-5.757	-9.249
M-97-6	5.0	4.5	0.5	2E-05	-10.14	-12.59	-22.67	-6.42	-4.97	-5.08	N/A	N/A	-12.12	-9.01	-8.64	-4.80	-5.51	-17.09	-6.733	-10.11
M-97-5	4.8	4.5	0.3	1E-04	-8.86	-11.33	-21.41	-5.33	-4.05	-4.35	N/A	N/A	-11.95	-9.02	-8.04	-4.02	-4.56	-16.67	-5.179	-8.733
Pourtier et al. (2010) at 550 °C and 2 kbar, in H_2O																				
M-98-3	5.2	4.5	0.7	1E-04	-10.38	-10.49	-21.33	-5.85	-4.05	-4.26	N/A	N/A	-10.97	-9.04	-8.8	-4.24	-4.33	-18.01	-4.794	-8.83
M-98-14	5.1	4.5	0.6	3E-04	-9.88	-10.04	-20.92	-5.41	-3.68	-3.95	N/A	N/A	-10.96	-9.09	-8.62	-3.99	-4.02	-17.9	-4.31	-8.409

Pourtier et al. (2010) at 625 °C and 2 kbar, in H_2O																			
M-98-34	5.3	4.5	0.8	8E-04	-10.4	-9.34	-21.31	-5.33	-3.29	-3.57	N/A	N/A	-10.73	-9.67	-9.12	-4.04	-3.66	-18.89	-3.847	-8.372
Pourtier et al. (2010) at 700 °C and 2 kbar, in H_2O																			
M-98-5	5.7	4.5	1.2	3E-04	-11.96	-9.27	-21.87	-6.18	-3.68	-3.8	N/A	N/A	-10.25	-9.81	-9.82	-4.47	-3.87	-19.86	-4.208	-8.969
M-98-1	5.8	4.5	1.3	2E-04	-12.17	-9.3	-21.73	-6.36	-3.83	-3.91	N/A	N/A	-10.11	-9.64	-9.86	-4.55	-3.98	-19.88	-4.354	-9.084
Pourtier et al. (2010) at 300 °C and 2 kbar in H_2O-NaCl-HCl-NaOH system																			
Nd-05-21	2.4	2.4	0	1.4	-9.66	-6.72	-6.82	-10.19	-11.98	-14.7	-7.27	-0.18	-2.46	-0.16	-11.48	-6.18	-5.27	-21.28	-10.9	-15.8
Nd-05-19	2.0	2	0	0.8	-8.82	-6.11	-6.45	-9.75	-11.95	-15.07	-7.92	-0.66	-2.28	-0.39	-11.8	-6.09	-4.76	-22.02	-10.73	-16.08
Nd-03-10	5.9	6.1	0.2	0.35	-11.27	-8.88	-9.54	-8.25	-6.52	-5.69	-4.28	-1.28	-6.54	-0.71	-7.66	-5.89	-8.5	-13.94	-10.33	-11.75
Nd-04-18	7.4	7.5	0.1	0.19	-14.98	-12.83	-13.71	-10.52	-7.34	-5.06	-3.06	-1.74	-8.21	-0.94	-6.14	-5.80	-9.86	-10.97	-10.17	-10.15
Nd-04-12	7.9	8	0.1	0.19	-16.31	-14.17	-15.07	-11.33	-7.64	-4.85	-2.55	-1.75	-8.74	-0.96	-5.82	-6.00	-10.57	-10.14	-10.56	-10.03
Nd-04-14	6.9	7	0.1	0.18	-14.17	-12.03	-12.93	-10.18	-7.48	-5.68	-3.55	-1.76	-7.75	-0.95	-6.94	-6.14	-9.72	-12.25	-10.83	-11.28
Nd-04-11	3.0	3	0	0.18	-8.73	-6.59	-7.48	-8.66	-9.89	-12	-7.47	-1.76	-3.83	-0.95	-10.94	-6.22	-5.88	-20.17	-10.99	-15.36
Nd-03-8	7.4	7.5	0.1	0.19	-15.54	-13.4	-14.3	-11.07	-7.89	-5.6	-3.06	-1.76	-8.24	-0.95	-6.66	-6.34	-10.4	-11.48	-11.23	-11.2
Nd-03-6	5.1	4.9	0.2	0.18	-9.09	-6.95	-7.85	-6.91	-6.02	-6.03	-5.36	-1.77	-5.94	-0.95	-8.2	-5.58	-7.35	-15.32	-9.727	-11.99
Nd-03-5	1.0	1	0	0.19	-7.15	-4.99	-5.88	-9.11	-12.37	-16.52	-11	-3.24	-1.78	-0.94	-13.17	-6.41	-4.03	-24.43	-11.38	-17.78
Nd-03-4	4.5	4.4	0.1	0.19	-8.89	-6.73	-7.61	-7.34	-7.07	-7.7	-5.97	-1.73	-5.3	-0.94	-9.13	-5.90	-7.04	-16.88	-10.35	-13.24
Nd-03-3	2.2	2.2	0	0.19	-8.17	-6.02	-6.91	-8.9	-10.91	-13.82	-8.28	-1.77	-3.03	-0.94	-11.76	-6.24	-5.11	-21.78	-11.05	-16.21
Pourtier et al. (2010) at 650 °C and 5 kbar in H_2O-NaCl-HCl-NaOH system																			
Nd-03-2	5.8	5	0.8	0.15	-13.11	-4.38	-9.52	-8.01	-5.84	-5.73	-3.13	-1.31	-4.18	-1.09	-7.54	-4.50	-6.03	-15.19	-4.747	-7.398
Pourtier et al. (2010) at 650 °C and 2 kbar in H_2O-NaCl-HCl-NaOH-H_3PO_4 system																			
NdA1	3.8	4	0.2	0.11	-17.01	-7.37	-11.53	-13.34	-12.79	-14.67	-5.93	-0.98	-0.89	-1.69	-10.83	-4.01	-1.91	-22.34	-3.617	-9.87
NdA2	4	4	0	0.07	-16.54	-6.77	-10.79	-12.65	-11.88	-13.54	-5.75	-0.89	-0.98	-1.56	-10.99	-4.39	-2.51	-22.28	-4.38	-10.41
NdA3	4.1	4	0.1	0.07	-15.31	-5.53	-9.54	-11.39	-10.6	-12.23	-5.74	-0.89	-1	-1.55	-11.59	-5.01	-3.16	-22.85	-5.623	-11.63
Pourtier et al. (2010) at 650 °C and 2 kbar by weight loss method																			
BK16	3.6	3.5	0.1	0.13	-14.89	-4.94	-8.78	-11.46	-11.15	-13.26	-6.06	-0.55	-0.34	-1.37	-12.57	-5.51	-3.18	-24.31	-6.618	-13.1
BK15	3.6	3.5	0.1	0.13	-14.61	-4.66	-8.49	-11.17	-10.86	-12.96	-6.06	-0.55	-0.35	-1.37	-12.32	-5.27	-2.95	-24.06	-6.139	-12.62
BK14	3.6	3.5	0.1	0.13	-15.05	-5.1	-8.94	-11.62	-11.31	-13.42	-6.06	-0.55	-0.34	-1.37	-12.7	-5.65	-3.31	-24.45	-6.886	-13.37
BK5	6.5	6	0.5	0.13	-14.86	-4.91	-8.76	-8.49	-5.25	-4.43	-3.12	-0.56	-3.28	-1.38	-8.94	-4.82	-5.42	-17.75	-5.238	-8.792
BK6	5.1	5	0.1	0.13	-14.77	-4.82	-8.67	-9.78	-7.91	-8.46	-4.5	-0.56	-1.91	-1.38	-10.3	-4.80	-4.02	-20.48	-5.191	-10.12
BK4	4.6	4.5	0.1	0.13	-15	-5.05	-8.9	-10.55	-9.22	-10.31	-5.04	-0.56	-1.36	-1.38	-11.03	-5.00	-3.68	-21.76	-5.587	-11.06
Van Hoozen et al. (2020) at 100 °C and Psat																			

NdPO4-8	2.0	2.0	0.01	0.01	-7.23	0.00	0.00	-11.83	-16.42	-21.36	N/A	N/A	N/A	N/A	-10.02	-4.75	-4.18	-20.11	-10.61	-15.3
NdPO4-7	2.0	2.0	0.01	0.01	-7.49	0.00	0.00	-12.08	-16.68	-21.62	N/A	N/A	N/A	N/A	-10.09	-4.83	-4.26	-20.19	-10.76	-15.45
NdPO4-6	2.0	2.0	0.01	0.01	-7.47	0.00	0.00	-12.06	-16.66	-21.59	N/A	N/A	N/A	N/A	-10.15	-4.88	-4.31	-20.24	-10.87	-15.56
NdPO4-5	2.0	2.0	0.01	0.01	-7.69	0.00	0.00	-12.30	-16.92	-21.87	N/A	N/A	N/A	N/A	-10.08	-4.80	-4.21	-20.20	-10.71	-15.41
NdPO4-4	2.0	2.0	0.01	0.01	-7.07	0.00	0.00	-11.66	-16.26	-21.20	N/A	N/A	N/A	N/A	-10.48	-5.22	-4.65	-20.58	-11.54	-16.22
NdPO4-3	2.0	2.0	0.01	0.01	-7.58	0.00	0.00	-12.17	-16.77	-21.71	N/A	N/A	N/A	N/A	-10.13	-4.87	-4.30	-20.23	-10.84	-15.53
NdPO4-2	2.0	2.0	0.01	0.01	-7.83	0.00	0.00	-12.43	-17.02	-21.96	N/A	N/A	N/A	N/A	-10.23	-4.96	-4.39	-20.32	-11.03	-15.72
NdPO4-1	2.0	2.0	0.01	0.01	-8.20	0.00	0.00	-12.79	-17.39	-22.33	N/A	N/A	N/A	N/A	-10.20	-4.94	-4.37	-20.30	-10.98	-15.67
Van Hoozen et al. (2020) at 150 °C and Psat																				
NdPO4-11	2.0	2.0	0.02	0.01	-7.43	0.00	0.00	-10.54	-14.16	-18.26	N/A	N/A	N/A	N/A	-10.65	-5.14	-4.25	-20.90	-10.65	-15.57
NdPO4-10	2.0	2.0	0.02	0.01	-7.83	0.00	0.00	-10.94	-14.56	-18.66	N/A	N/A	N/A	N/A	-10.71	-5.20	-4.31	-20.96	-10.77	-15.69
NdPO4-9	2.0	2.0	0.02	0.01	-7.47	0.00	0.00	-10.58	-14.20	-18.30	N/A	N/A	N/A	N/A	-10.63	-5.13	-4.23	-20.88	-10.62	-15.54
Van Hoozen et al. (2020) at 200 °C and Psat																				
NdPO4-14	2.0	2.0	0.03	0.01	-8.45	0.00	0.00	-10.37	-13.26	-16.81	N/A	N/A	N/A	N/A	-11.05	-5.22	-3.99	-21.59	-10.13	-15.37
NdPO4-13	2.0	2.0	0.03	0.01	-8.49	0.00	0.00	-10.40	-13.29	-16.84	N/A	N/A	N/A	N/A	-11.10	-5.27	-4.03	-21.63	-10.23	-15.46
NdPO4-12	2.0	2.0	0.03	0.01	-8.58	0.00	0.00	-10.50	-13.38	-16.94	N/A	N/A	N/A	N/A	-11.08	-5.25	-4.02	-21.62	-10.19	-15.43
Van Hoozen et al. (2020) at 250 °C and Psat																				
NdPO4-16	2.1	2.0	0.04	0.01	-8.54	0.00	0.00	-9.48	-11.80	-15.01	N/A	N/A	N/A	N/A	-12.03	-5.77	-4.13	-23.01	-10.61	-16.27
NdPO4-15	2.1	2.0	0.04	0.01	-8.96	0.00	0.00	-9.90	-12.22	-15.44	N/A	N/A	N/A	N/A	-12.01	-5.74	-4.10	-22.98	-10.55	-16.22

[1] The predicted equilibrium pH at experimental temperatures and pressures

[2] The equilibrium pH reported in the respective studies

[3] The difference between the reported pH in the previous studies and the recalculated equilibrium pH for the respective studies using the updated database.